AGU PUBLICATIONS

Water Resources Research

RESEARCH ARTICLE
10.1002/2016WR019907

Key Points:
- Simple elevation-based downscaling methods for average precipitation and potential evapotranspiration are proposed
- Much of the spatial variability in average precipitation and PET is captured for the Reynolds Creek watershed
- Spatial variations in precipitation and PET affect soil moisture patterns and improve soil moisture downscaling

Correspondence to:
J. D. Niemann,
jniemann@engr.colostate.edu

Citation:
Cowley, G. S., J. D. Niemann, T. R. Green, M. S. Seyfried, A. S. Jones, and P. J. Grazaitis (2017), Impacts of precipitation and potential evapotranspiration patterns on downscaling soil moisture in regions with large topographic relief, *Water Resour. Res.*, *53*, 1553–1574, doi:10.1002/2016WR019907.

Received 7 OCT 2016
Accepted 21 JAN 2017
Accepted article online 27 JAN 2017
Published online 21 FEB 2017

Impacts of precipitation and potential evapotranspiration patterns on downscaling soil moisture in regions with large topographic relief

Garret S. Cowley[1], Jeffrey D. Niemann[1], Timothy R. Green[2], Mark S. Seyfried[3], Andrew S. Jones[4], and Peter J. Grazaitis[5]

[1]Department of Civil and Environmental Engineering, Colorado State University, Fort Collins, Colorado, USA, [2]Center for Agricultural Resources Research, Agricultural Research Service, USDA, Fort Collins, Colorado, USA, [3]Northwest Watershed Research Center, Agricultural Research Service, USDA, Boise, Idaho, USA, [4]Cooperative Institute for Research in the Atmosphere, Colorado State University, Fort Collins, Colorado, USA, [5]U.S. Army Research Development, and Engineering Command, Army Research Laboratory, Adelphi, Maryland, USA

Abstract Soil moisture can be estimated at coarse resolutions (>1 km) using satellite remote sensing, but that resolution is poorly suited for many applications. The Equilibrium Moisture from Topography, Vegetation, and Soil (EMT+VS) model downscales coarse-resolution soil moisture using fine-resolution topographic, vegetation, and soil data to produce fine-resolution (10–30 m) estimates of soil moisture. The EMT+VS model performs well at catchments with low topographic relief (≤124 m), but it has not been applied to regions with larger ranges of elevation. Large relief can produce substantial variations in precipitation and potential evapotranspiration (PET), which might affect the fine-resolution patterns of soil moisture. In this research, simple methods to downscale temporal average precipitation and PET are developed and included in the EMT+VS model, and the effects of spatial variations in these variables on the surface soil moisture estimates are investigated. The methods are tested against ground truth data at the 239 km^2 Reynolds Creek watershed in southern Idaho, which has 1145 m of relief. The precipitation and PET downscaling methods are able to capture the main features in the spatial patterns of both variables. The space-time Nash-Sutcliffe coefficients of efficiency of the fine-resolution soil moisture estimates improve from 0.33 to 0.36 and 0.41 when the precipitation and PET downscaling methods are included, respectively. PET downscaling provides a larger improvement in the soil moisture estimates than precipitation downscaling likely because the PET pattern is more persistent through time, and thus more predictable, than the precipitation pattern.

1. Introduction

Volumetric soil water content (soil moisture) plays a central role in earth surface processes and connects the atmospheric, geomorphic, hydrologic, and biologic sciences [*Legates et al.*, 2011]. It is a principal variable in many watershed-scale processes including soil erosion [*Singh and Thompson*, 2016], crop yield [*Green and Erskine*, 2004], land-atmosphere interaction [*Entekhabi et al.*, 1996; *Pal and Eltahir*, 2001], and runoff generation [*Western et al.*, 2001; *Castillo et al.*, 2003; *Ruggenthaler et al.*, 2015]. Thus, reliable soil moisture data at watershed scales would benefit many applications that are impacted by these processes.

Satellite remote sensing methods allow monitoring of soil moisture over suitably large spatial extents. Such methods include the Advanced Scatterometer (ASCAT) [*Figa-Saldana et al.*, 2002], the Advanced Microwave Scanning Radiometer E (AMSR-E) [*Njoku et al.*, 2003], WindSat [*Li et al.*, 2010], and the more recent NASA Soil Moisture Active and Passive (SMAP) [*Entekhabi et al.*, 2010]. However, these satellites provide soil moisture values at resolutions ranging from 5 to 60 km. Most watershed-scale applications require much finer-resolution soil moisture (10–30 m), so downscaling is needed.

Many soil moisture downscaling methods have been proposed, and they vary in formulation and in the supplemental data that they use to infer fine-scale variations of soil moisture. Some downscaling methods have been designed to use optical/thermal or radar backscatter data that are commonly available from satellite

observation systems [*Chauhan et al*., 2003; *Merlin et al*., 2005; *Merlin et al*., 2006; *Das et al*., 2014; *Song et al*., 2014; *Peng et al*., 2016]. These methods typically produce soil moisture estimates with resolutions of 1 km or larger due to the resolution of the ancillary data they use. For example, *Peng et al*. [2016] proposed a soil moisture downscaling method based on land surface temperature (LST) and the vegetation temperature condition index to produce soil moisture at a resolution of 5.6 km. This approach requires a relatively flat region because it assumes that variations in surface temperature are caused by evaporative cooling rather than variations in elevation. Other downscaling methods use statistical relationships and interpolation techniques [*Crow et al*., 2000; *Kim and Barros*, 2002; *Kaheil et al*., 2008; *Mascaro et al*., 2010]. These methods primarily focused on the statistical properties of fine-scale soil moisture and how they can be empirically estimated from ancillary data.

Another class of downscaling methods use topographic and vegetation data because these variables have been shown to be related to fine-scale soil moisture variations [*Western et al*., 1999; *Gomez-Plaza et al*., 2001; *Brocca et al*., 2007; *Traff et al*., 2015]. These downscaling methods often reach 10–30 m resolutions, but they typically have been applied to small catchments with low topographic relief. *Wilson et al*. [2005] developed an empirical downscaling technique that uses fine-scale topographic attributes such as elevation, specific contributing area, slope, wetness index, potential solar radiation index (PSRI), lowness, and a multiresolution valley bottom flatness index. The method was applied to catchments with less than 80 m of topographic relief. *Pellenq et al*. [2003] developed a method to disaggregate soil moisture based on fine-scale topography and soil depth using a modification of TOPMODEL [*Beven and Kirkby*, 1979]. They also applied the downscaling method to a catchment with low relief (27 m). *Temimi et al*. [2010] proposed a downscaling method that combines TOPMODEL's wetness index with remotely sensed vegetation data and applied it to a very large region with about 85 m of topographic relief, but the effects of elevation on soil moisture were not considered. *Ranney et al*. [2015] used a water balance approach called the Equilibrium Moisture from Topography, Vegetation and Soil (EMT+VS) model to downscale soil moisture. The model uses fractional vegetation cover along with slope, curvature, specific contributing area, and PSRI to infer the fine-scale variations in soil moisture. Application of the EMT+VS model has also been limited to catchments with low topographic relief ($\leq$124 m).

In a large watershed or region (e.g., a 5–60 km soil moisture grid cell from a satellite product), elevation can vary greatly, which might produce spatial variations in soil moisture due to spatial variations in climate. In particular, elevation is known to affect spatial patterns of precipitation, and many studies have developed methods to interpolate precipitation using elevation data [*Chua and Bras*, 1982; *Hevesi et al*., 1992; *Phillips et al*., 1992; *Garen et al*., 1994; *Lloyd*, 2005]. *Kyriakidis et al*. [2001] showed how spatial patterns of precipitation are related to atmospheric and terrain characteristics such as elevation, specific humidity, and wind speed. Geostatistical kriging methods that use elevation as a secondary variable have been shown to produce better estimations of annual and monthly rainfall [*Goovaerts*, 2000] as well as daily rainfall [*Ly et al*., 2011] than deterministic methods that do not incorporate elevation. The orographic relationship between elevation and precipitation can also be affected by other topographic attributes. *Hanson* [1982] and *Garen et al*. [1994] found that the relationship between elevation and precipitation differs for opposing sides of the Reynolds Creek watershed. *Spreen* [1947] found that precipitation in Colorado is correlated with elevation, slope, exposure, and aspect. Elevation alone explains 30% of the total variance in precipitation, and the four attributes together explain 88% of the variance. *Daly et al*. [1994] and *Prudhomme and Reed* [1999] incorporated topographic factors such as orientation categories to capture windward and leeward effects on precipitation patterns.

Elevation can also affect air temperature [*Leemans and Cramer*, 1991; *Willmott and Matsuura*, 1995; *Dodson and Marks*, 1997; *Sun and Zhang*, 2016], which impacts the spatial distribution of potential evapotranspiration (PET), evapotranspiration (ET), and possibly soil moisture. *Shevenell* [1999] demonstrated that pan evaporation decreases approximately linearly with elevation in the arid climate of Nevada. *Vanderlinden et al*. [2008] found a similar relationship between elevation and reference crop ET for the mountainous region of Andalusia, Spain. They found that estimation of annual reference crop ET improves significantly when elevation data are used. Monthly PET also has a strong inverse relationship with elevation in the mountainous Lhasa River basin in China [*Shi et al*., 2014].

The dependence of precipitation and PET (or temperature) on elevation has been suggested to impact soil moisture variability. *Seyfried* [1998] observed that soil moisture generally increases with elevation in the

Reynolds Creek watershed, and *Seyfried et al*. [2011] further investigated the climatic variations related to elevation that impact the soil moisture trends. *Jawson and Niemann* [2006] investigated soil moisture patterns in Oklahoma over varying spatial extents using an empirical orthogonal function (EOF) analysis. They found that elevation is typically among the most important characteristics in determining soil moisture patterns. *Qiu et al*. [2014] performed a similar EOF analysis in China and found that watershed-scale soil moisture patterns are most strongly correlated to topographic attributes such as elevation and slope.

The objective of this paper is to investigate the influence of orographic precipitation and PET patterns on soil moisture downscaling in regions with large topographic relief. New precipitation and PET downscaling methods are proposed and evaluated using rain gauge and weather station data from the mountainous Reynolds Creek watershed. The two downscaling methods are then added to the EMT+VS model to evaluate how elevation-dependent precipitation and PET affect the fine-scale estimates of soil moisture. The EMT+VS model is used because it has the strongest physical basis among available topographic downscaling methods. For example, it has been shown to reproduce both valley-dependent and hillslope-dependent soil moisture patterns, and it can reproduce temporally unstable soil moisture patterns [*Coleman and Niemann*, 2013]. The model also outperforms a purely statistical downscaling method when calibration data are limited [*Werbylo and Niemann*, 2014], suggesting that the process conceptualizations help constrain the model to more realistic behavior.

2. Methodology

2.1. Preexisting Model Components

Ranney et al. [2015] provides a detailed explanation and derivation of the EMT+VS model, but an overview of the preexisting model components is provided here. The EMT+VS model considers the water balance of the hydrologically active layer, which is defined as the depth of soil through which lateral flow can occur. Ultimately, the soil moisture is calculated by assuming equilibrium between the inflows and outflows for this layer. The soil moisture that is being downscaled is expected to vary in time, which ultimately produces temporal variability in the fine-scale soil moisture output. However, any direct dependence on time is neglected in the model when inferring the spatial variations for downscaling. Four processes are simulated in the water balance: infiltration F, deep drainage G, lateral flow L, and ET E.

Infiltration F (mm/d) is described using a simple linear function that accounts for interception by vegetation cover

$$F = F_0(1-\lambda V), \tag{1}$$

where F_0 (mm/d) is a spatially constant reference precipitation rate, which is typically considered the temporal average precipitation for the application region. The term in parentheses represents the throughfall. The parameter λ represents the interception efficiency of the vegetation cover, and V is the fractional vegetation cover, which is assumed to be known at the fine resolution.

Deep drainage G (mm/d) is described using Darcy's Law, a percolation assumption, and the *Campbell* [1974] equation for unsaturated hydraulic conductivity. It is written

$$G = K_{s,v}\left(\frac{\theta}{\phi}\right)^{\gamma_v}, \tag{2}$$

where $K_{s,v}$ (mm/d) is the vertical saturated hydraulic conductivity, θ is the volumetric water content in the modeled layer, ϕ is the soil porosity, and γ_v is the vertical pore disconnectedness index.

Lateral flow L (m^2 mm/d) is modeled using Darcy's law, a soil depth that depends on topographic curvature, the *Campbell* [1974] equation for unsaturated hydraulic conductivity, and the assumption that the hydraulic gradient is a power function of topographic slope. The resulting expression is

$$L = \delta_0\left(\frac{\kappa_{\min}-\kappa}{\kappa_{\min}}\right)cIK_{s,v}\left(\frac{\theta}{\phi}\right)^{\gamma_h}S^{\varepsilon}, \tag{3}$$

where δ_0 (m) is the thickness of the hydrologically active layer at locations where topographic curvature is zero, $\kappa_{\min}$ is the minimum topographic curvature for which the hydrologically active layer is present, κ is

the topographic curvature from the fine-resolution digital elevation model (DEM), c (m) is the length of the DEM grid cell (which is also the resolution of the final soil moisture estimates), ι is the anisotropy of saturated hydraulic conductivity, γ_h is the horizontal pore disconnectedness index, S is the topographic slope from the DEM, and ε is a parameter that relates the horizontal hydraulic gradient to topographic slope.

The equation for ET E (mm/d) uses the *Priestly and Taylor* [1972] assumption and power functions to describe the effects of limited moisture on the ET rate. It includes shading effects and allows root-water uptake from other (nonmodeled) soil layers. It is written

$$E=E_p[\eta V+(1-V)^{\mu}]\left[\frac{I_p}{1+\alpha}\left(\frac{\theta}{\phi}\right)^{\beta_r}+\frac{\alpha}{1+\alpha}\left(\frac{\theta}{\phi}\right)^{\beta_a}\right], \tag{4}$$

where E_p (mm/d) is the temporal average PET, η is the portion of transpiration that is contributed by the hydrologically active layer, μ accounts for shading effects on soil evaporation, α is the Priestly-Taylor coefficient minus one, and β_r and β_a characterize the moisture limitation effect in the radiative and aerodynamic terms of E, respectively. I_p is the PSRI from the fine-resolution DEM.

2.2. Precipitation Downscaling

The precipitation downscaling method aims to replace the spatially constant temporal average precipitation F_0 with a simple model that allows for spatial variations in this variable. The downscaling method is based on four assumptions about the relationship between the precipitation and topography. First, spatial variations in precipitation are assumed to depend linearly on elevation. Linear dependence has been observed and implemented by numerous previous studies [*Chua and Bras*, 1982; *Daly et al*., 1994; *Garen et al*., 1994; *Goovaerts*, 2000; *Castro et al*., 2014]. Second, spatial variations in precipitation are also assumed to depend linearly on topographic aspect with respect to wind direction (referred to as topographic orientation for simplicity) as observed/implemented by *Basist et al*. [1994], *Kyriakidis et al*. [2001], *Guan et al*. [2005], and *Franke et al*. [2008]. Third, the dependences on elevation and orientation are assumed to interact as observed by *Hanson* [1982]. Fourth, the spatial scale at which these relationships are strongest is assumed to be larger than typical DEM resolutions. Previous studies have evaluated precipitation-topography relationships at varying spatial resolutions [*Thornton et al*., 1997; *Foresti and Pozdnoukhov*, 2012]. For example, *Thornton et al*. [1997] found that elevation data at resolutions between 2 and 8 km produce the strongest relationships with precipitation. Similarly, the Precipitation-elevation Regression on Independent Slopes Model (PRISM) describes the topography using a 6 km by 9 km resolution [*Daly et al*., 1994].

Using these four assumptions, a heuristic precipitation downscaling method can be written as

$$P=\bar{P}\frac{\left[1+\tau\left(Z_{\#}-\bar{Z}_{\#}\right)\right]\left\{1+\xi\left[S_{\#}\cos\left(R_{\#}-v\right)-\overline{S_{\#}\cos\left(R_{\#}-v\right)}\right]\right\}}{1+\tau\xi\left(\overline{Z_{\#}S_{\#}\cos\left(R_{\#}-v\right)}-\bar{Z}_{\#}\overline{S_{\#}\cos\left(R_{\#}-v\right)}\right)}, \tag{5}$$

where P (mm/d) is the local precipitation, $\bar{P}$ (mm/d) is the spatial average precipitation, τ (1/m) is a parameter that controls the elevation dependence, ξ is a parameter that controls the orientation dependence, and v is a reference direction from which all topographic orientations are calculated. The parameter v is expected to be related to the prevailing wind direction. The variables $Z_{\#}$ (m), $S_{\#}$, and $R_{\#}$ are the average elevation, slope, and aspect within a square neighborhood around the grid cell of interest. Note that average aspect must be calculated by determining the arctangent of the ratio between the sums of the sines and cosines of the aspects within the neighborhood. The spatial extent of the neighborhood is the spatial scale at which orographic precipitation effects occur (i.e., the 2–8 km scale found by *Thornton et al*. [1997]). For simplicity, we refer to these variables as the orographic elevation, slope, and aspect. The overbars in equation (5) indicate spatial averages of the attributes and attribute combinations over the entire downscaling region (e.g., the watershed or a coarse-resolution grid cell).

The first term in the numerator of equation (5) represents the linear dependence of precipitation on elevation. The second term in the numerator describes the linear dependence on orientation. The orographic slope $S_{\#}$ is included in the second term because the orientation is expected to have a greater effect on precipitation if the surface has a larger slope, which is similar to what was done by *Basist et al*. [1994]. The

multiplication of the two terms in the numerator allows the two topographic dependencies to interact. The denominator is simply a constant that ensures that the supplied spatial average precipitation $\bar{P}$ is preserved after downscaling for any given collection of orographic elevations, slopes, and aspects.

The downscaled precipitation can be included in the EMT+VS model by replacing the reference precipitation F_0 in equation (1). The modified infiltration term becomes

$$F=\bar{P}\frac{\left[1+\tau\left(Z_{\#}-\bar{Z}_{\#}\right)\right]\left\{1+\xi\left[S_{\#}\cos\left(R_{\#}-v\right)-\overline{S_{\#}\cos\left(R_{\#}-v\right)}\right]\right\}}{1+\tau\xi\left[\overline{Z_{\#}S_{\#}\cos\left(R_{\#}-v\right)}-\bar{Z}_{\#}\overline{S_{\#}\cos\left(R_{\#}-v\right)}\right]}\left(1-\lambda V\right). \tag{6}$$

The mathematical implications of this change to the model will be described in section 2.4.

2.3. PET Downscaling

The PET downscaling method begins by assuming that the temporal average PET depends linearly on air temperature, similar to the Blaney-Criddle equation [*Blaney and Criddle*, 1950], which has been shown to provide comparable results to other PET methods [*Oudin et al*., 2005]. Specifically, the Blaney-Criddle equation can be written

$$E_p=K_1^*T+K_2^*, \tag{7}$$

where K_1^* and K_2^* are empirical coefficients that depend in part on the relative number of daylight hours and thus are expected to vary between different regions [*Doorenbos and Pruitt*, 1977]. Because daylight hours are not tracked in the EMT+VS model, the two coefficients are instead assumed to be linear functions of spatial average PET $\bar{E}_p$ as follows:

$$K_1^*=K_1\bar{E}_p, \tag{8}$$

$$K_2^*=K_2\bar{E}_p, \tag{9}$$

where K_1 and K_2 are two parameters. This assumption is similar to the approaches of *Ekström et al*. [2007] and *Sperna Weiland et al*. [2012] who modified the Blaney-Criddle equation so that the coefficients could vary spatially to account for climate variability.

Within the troposphere, ambient air temperature varies approximately linearly with altitude according to

$$T=T_r-\psi Z, \tag{10}$$

where T_r (°C) is the temperature at sea level, ψ (°C/m) is the environmental or ambient lapse rate, and Z (m) is altitude. According to *Bras* [1990], the ambient lapse rate is typically between 5 and 8°C/km. Neutral or average temperature gradients have been suggested to be about 6°C/km [*Dodson and Marks*, 1997], and *Rolland* [2003] found an average of about 5.6°C/km for the mountainous region of northern Italy. If we assume that the dependence of air temperature on altitude also describes the dependence of surface air temperature on elevation (similar to *Leemans and Cramer* [1991]), then equations (7) and (10) can be combined as

$$\frac{E_p}{\bar{E}_p}=K_1\left(T_r-\psi Z\right)+K_2, \tag{11}$$

where Z now represents topographic elevation. Calculating the spatial average of this equation within the downscaling region, one gets

$$\frac{\bar{E}_p}{\bar{E}_p}=\frac{1}{A_c}\int K_1T_r dA_c-\frac{1}{A_c}\int K_1\psi Z dA_c+\frac{1}{A_c}\int K_2 dA_c, \tag{12}$$

where A_c (m^2) is the area of the region. For simplicity, we assume that T_r, ψ, K_1, and K_2 are spatially constant within the downscaling region, so we get

$$1+K_1\psi\bar{Z}=K_1T_r+K_2, \tag{13}$$

where $\bar{Z}$ (m) is the average elevation in the region. Also, equation (11) can be rearranged as

$$\frac{E_p}{\bar{E}_p}+K_1\psi Z=K_1T_r+K_2. \tag{14}$$

Combining equations (13) and (14) and solving for E_p, one gets

$$E_p=\bar{E}_p+\bar{E}_pK_1\psi(\bar{Z}-Z). \tag{15}$$

This equation provides a simple way to downscale the spatial average PET using fine-scale variations in elevation. Because K_1 and ψ appear together in the equation and are both unknown parameters, they can be combined into a single parameter ω (1/m). Together, ω and $\bar{E}_p$ control the dependence of PET on elevation. Equation (15) can be incorporated into the EMT+VS model by substituting for E_p in equation (4), which becomes

$$E=\overline{E}_p\left[1+\omega\left(\overline{Z}-Z\right)\right]\left[\eta V+(1-V)^{\mu}\right]\left[\frac{I_p}{1+\alpha}\left(\frac{\theta}{\phi}\right)^{\beta_r}+\frac{\alpha}{1+\alpha}\left(\frac{\theta}{\phi}\right)^{\beta_a}\right]. \tag{16}$$

The first bracketed term now allows the local PET to vary with elevation.

2.4. Resulting Soil Moisture Equation

Coleman and Niemann [2013] and *Ranney et al*. [2015] developed and tested a solution to the water balance equation by which local soil moisture can be calculated from a known spatial average soil moisture. In this method, explicit analytical solutions for soil moisture are first obtained by assuming that each outflow term in the water balance dominates for the date when downscaling is performed. Then, the final soil moisture estimate is calculated by a weighted average of the analytical solutions, where the weights are found from the magnitudes of the outflow terms in the water balance equation (equations (2), (3), and (16)). The same approach is used for the model when precipitation and PET downscaling are included, which produces the following estimate of the local or fine-scale soil moisture:

$$\theta=\frac{w_G\theta_G+w_L\theta_L+w_R\theta_R+w_A\theta_A}{w_G+w_L+w_R+w_A}, \tag{17}$$

where θ_G, θ_L, θ_R, and θ_A are the explicit soil moisture estimates if deep drainage, lateral flow, radiative ET, and aerodynamic ET dominate, respectively, and w_G, w_L, w_R, and w_A are associated weights. The equations for θ_G, θ_L, θ_R, and θ_A are

$$\theta_G=\bar{\theta}\frac{\mathrm{DDI}}{\overline{\mathrm{DDI}}}, \tag{18}$$

$$\theta_L=\bar{\theta}\frac{\mathrm{LFI}}{\overline{\mathrm{LFI}}}, \tag{19}$$

$$\theta_R=\bar{\theta}\frac{\mathrm{REI}}{\overline{\mathrm{REI}}}, \tag{20}$$

$$\theta_A=\bar{\theta}\frac{\mathrm{AEI}}{\overline{\mathrm{AEI}}}, \tag{21}$$

where $\bar{\theta}$ is the known spatial average soil moisture, DDI is the deep drainage index, LFI is the lateral flow index, REI is the radiative ET index, and AEI is the aerodynamic ET index. The quantities $\overline{\mathrm{DDI}}$, $\overline{\mathrm{LFI}}$, $\overline{\mathrm{REI}}$, and $\overline{\mathrm{AEI}}$ are the spatial averages of the indices. The weights are

$$w_G=\left(\frac{\bar{\theta}}{\overline{\mathrm{DDI}}}\right)^{\gamma_v}, \tag{22}$$

$$w_L=\left(\frac{\bar{\theta}}{\overline{\mathrm{LFI}}}\right)^{\gamma_h}, \tag{23}$$

$$w_R=\left(\frac{\bar{\theta}}{\overline{\mathrm{REI}}}\right)^{\beta_r}, \tag{24}$$

$$w_A = \left(\frac{\bar{\theta}}{\overline{\mathrm{AEI}}}\right)^{\beta_a}. \tag{25}$$

Using the generalized infiltration and ET models (equations (6) and(16)) and following the solution method provided by *Coleman and Niemann* [2013] and *Ranney et al*. [2015], the indices can be calculated as follows:

$$\mathrm{DDI} \equiv \phi \frac{\left[1+\tau\left(Z_\# - \bar{Z}_\#\right)\right]^{1/\gamma_v}\left\{1+\xi\left[S_\#\cos\left(R_\# - v\right) - \overline{S_\#\cos\left(R_\# - v\right)}\right]\right\}^{1/\gamma_v}}{\left\{1+\tau\xi\left[\overline{Z_\# S_\#\cos\left(R_\# - v\right)} - \bar{Z}_\#\overline{S_\#\cos\left(R_\# - v\right)}\right]\right\}^{1/\gamma_v}}\left(\frac{1-\lambda V}{K_{s,v}}\right)^{1/\gamma_v}, \tag{26}$$

$$\mathrm{LFI} \equiv \phi \frac{\left[1+\tau\left(Z_\# - \bar{Z}_\#\right)\right]^{1/\gamma_h}\left\{1+\xi\left[S_\#\cos\left(R_\# - v\right) - \overline{S_\#\cos\left(R_\# - v\right)}\right]\right\}^{1/\gamma_h}}{\left\{1+\tau\xi\left[\overline{Z_\# S_\#\cos\left(R_\# - v\right)} - \bar{Z}_\#\overline{S_\#\cos\left(R_\# - v\right)}\right]\right\}^{1/\gamma_h}}\left(\frac{1-\lambda V}{\delta_0 \imath K_{s,v}}\right)^{1/\gamma_h}\left(\frac{A}{cS^e}\right)^{1/\gamma_h}\left(\frac{\kappa_{\min}}{\kappa_{\min}-\kappa}\right)^{1/\gamma_h}, \tag{27}$$

$$\mathrm{REI} \equiv \phi \frac{\left[1+\tau\left(Z_\# - \bar{Z}_\#\right)\right]^{1/\beta_r}\left\{1+\xi\left[S_\#\cos\left(R_\# - v\right) - \overline{S_\#\cos\left(R_\# - v\right)}\right]\right\}^{1/\beta_r}}{\left\{1+\tau\xi\left[\overline{Z_\# S_\#\cos\left(R_\# - v\right)} - \bar{Z}_\#\overline{S_\#\cos\left(R_\# - v\right)}\right]\right\}^{1/\beta_r}} \left\{\frac{1+\alpha}{\bar{E}_p[1+\omega(\bar{Z}-Z)]}\right\}^{1/\beta_r}\left(\frac{1}{I_p}\right)^{1/\beta_r}\left[\frac{(1-\lambda V)}{\eta V+(1-V)^\mu}\right]^{1/\beta_r} \tag{28}$$

$$\mathrm{AEI} \equiv \phi \frac{\left[1+\tau\left(Z_\# - \bar{Z}_\#\right)\right]^{1/\beta_a}\left\{1+\xi\left[S_\#\cos\left(R_\# - v\right) - \overline{S_\#\cos\left(R_\# - v\right)}\right]\right\}^{1/\beta_a}}{\left\{1+\tau\xi\left[\overline{Z_\# S_\#\cos\left(R_\# - v\right)} - \bar{Z}_\#\overline{S_\#\cos\left(R_\# - v\right)}\right]\right\}^{1/\beta_a}} \left\{\frac{1+\alpha}{\alpha\bar{E}_p[1+\omega(\bar{Z}-Z)]}\right\}^{1/\beta_a}\left[\frac{1-\lambda V}{\eta V+(1-V)^\mu}\right]^{1/\beta_a}. \tag{29}$$

These indices produce the spatial variations in the fine-scale soil moisture pattern. In the original EMT+VS model, those variations were produced by fine-scale variations in fractional vegetation cover V, slope S, curvature κ, PSRI I_p, and contributing area A. Now, they also depend on fine-scale variations in elevation Z and orographic elevation $Z_\#$, slope $S_\#$, and aspect $R_\#$. Z only appears in the REI and AEI because only those indices depend on the PET, but $Z_\#$, $S_\#$, and $R_\#$ appear in all four indices because these variables are associated with the input of water into the soil layer. The four soil moisture estimates θ_G, θ_L, θ_R, and θ_A are constant in time, but the four weights w_G, w_L, w_R, and w_A can vary because the supplied spatial average soil moisture $\bar{\theta}$ can change temporally.

The EMT+VS model has several features that contrast with conventional watershed models. It calculates the fine-resolution soil moisture from an explicit equation and directly accepts $\bar{\theta}$ as an input. It also requires no time step, no initial or preceding fine-resolution soil moisture pattern, and no time series of meteorological forcing data. This structure makes the model very computationally efficient and allows it to be applied to large regions at fine spatial resolutions. However, these benefits occur in part due to the equilibrium assumption, which means the EMT+VS model cannot capture any fine-scale features that are related to nonequilibrium conditions or hysteresis. The model also does not account for errors in the supplied $\bar{\theta}$ data.

3. Data Sets and Model Application

3.1. Data Sets Used for Model Evaluation

The precipitation and PET downscaling methods and the revised EMT+VS model are evaluated at the Reynolds Creek watershed, which is located in the Owyhee Mountains in southwestern Idaho [*Seyfried et al*., 2001]. The watershed has an area of 239 km^2 and 1145 m of relief (elevations range from 1100 to 2245 m). The annual average precipitation varies from about 230 mm at lower elevations to 1100 mm at higher elevations [*Hanson*, 2001], and average class A pan evaporation is about 1044 mm [*Hanson*, 1989]. Reynolds Creek is well-suited for this study because it has an extensive hydrologic monitoring network including rain gauges, weather stations, and soil moisture sensors. Furthermore, the stations are positioned to capture the

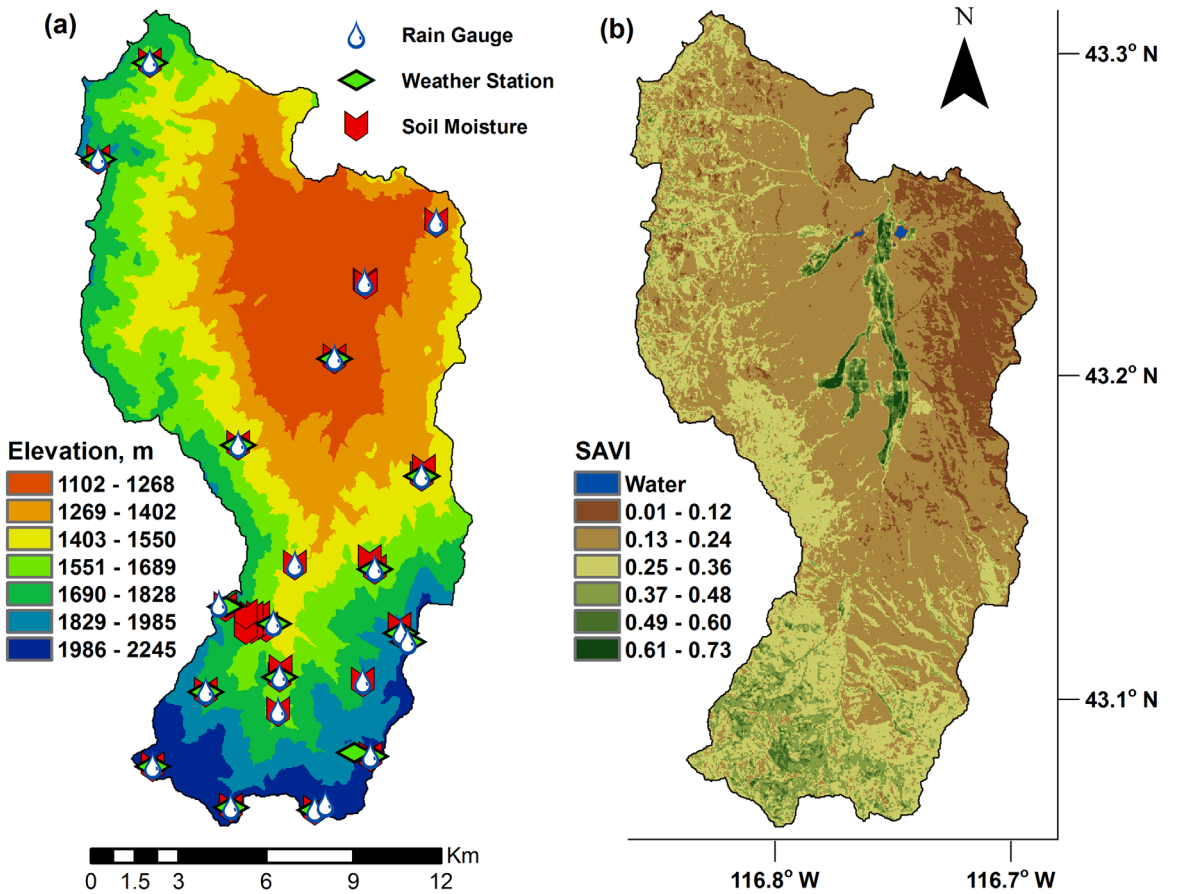

Figure 1. (a) Map of the Reynolds Creek watershed topography showing rain gauge, weather station, and soil moisture probe locations, and (b) map of Soil Adjusted Vegetation Index (SAVI) for the same watershed, which is used as fractional vegetation cover.

spatial variability of precipitation, PET, and soil moisture within the watershed. The data are all publicly available at ftp.nwrc.ars.usda.gov.

The rain gauge network includes 22 stations (Figure 1a) and data were available for 2012 through 2014. Each station has dual-gauged precipitation amounts at hourly time steps, which were then aggregated to obtain the average precipitation (total precipitation divided by total time including any interstorm periods) at each station. These precipitation values are expressed as rates (mm/d) throughout the study to be consistent with their use in the EMT+VS model.

The weather station network includes 17 stations that measure air temperature, vapor pressure, relative humidity, incoming solar radiation, and wind speed at a 15 min time interval (Figure 1a). Data were not yet available for 2014, so 2012 and 2013 were used to calculate PET. (The inconsistent time periods for precipitation and PET have little effect on the resulting estimates. If only 2012 and 2013 are used to estimate the average precipitation, the value changes by only 6%). The ASCE standardized reference ET equation [*ASCE-EWRI*, 2005], which is a version of the Penman-Montieth (P-M) equation [*Itenfisu et al.*, 2003], was used to estimate daily reference ET assuming a short grass reference crop. Daily PET was approximated with reference ET. The daily PET values were then used to obtain the average PET in each month of the year and the temporal average PET (mm/d) at each station.

The soil moisture network is comprised of 30 Hydra Probes (Figure 1a), which measure the soil moisture in the top ~5 cm of the soil layer with a measurement error of ± 0.03 m^3/m^3 [*Seyfried and Murdock*, 2004; *Seyfried et al.*, 2005]. These observations are assumed to characterize the soil moisture throughout the depth of the hydrologically active layer, which is estimated to be about 120 cm [*Seyfried et al.*, 2011], because deeper observations are unavailable. A total of 30 dates were selected for soil moisture downscaling from 2012 through 2015. The dates were selected to be as independent from each other as possible. Thus, they are

spread over four summers (the maximum allowed by the available observations), and they are always spaced by at least 8 days. Fall is avoided because the soil moisture is consistently dry in this period. Thus, including fall dates would add replicas of dry soil moisture patterns and reduce the independence between the dates. Winter is also excluded to avoid frozen soil. The selected dates capture a wide range of soil moisture conditions. The Hydra Probes record observations every 15 min or every hour, depending on the particular probe. The available data were used to calculate a daily average soil moisture at each station for each date of interest.

3.2. Model Inputs and Application

To apply the EMT+VS model, a spatial average soil moisture $\overline{\theta}$ is required as input. In this study, the average of the in situ soil moisture measurements was used. SMAP data could potentially be used but likely includes more error than the average of the in situ observations. Nonetheless, the average from the local observations is likely biased to wetter values because most stations occur at higher elevations in the watershed (Figure 1a).

A DEM is also required to calculate the fine-scale topographic attributes for the EMT+VS model (S, κ, A, I_p, Z, $Z_\#$, $S_\#$, and $R_\#$). A 30 m DEM was obtained from the United States Geological Survey (USGS) National Map Viewer. It is projected in universal transverse Mercator coordinates (zone 11) using the 1983 North American Datum and the GRS 1980 ellipsoid. Pits were removed and d-infinity flow directions were determined using the TauDEM Toolbox [*Tarboton*, 1997]. The resulting elevation map is shown in Figure 1a.

Fine-scale fractional vegetation cover V was also supplied to the EMT+VS model as a temporally constant variable. Landsat surface reflectance data at a 30 m resolution were obtained using USGS Earth Explorer. The reflectance data were used to derive the soil adjusted vegetation index (SAVI) [*Huete*, 1988], and SAVI values were directly used in the EMT+VS model as V. Vegetation indices like SAVI have been shown to be composite properties of vegetation that include both leaf area and canopy cover [*Glenn et al*., 2008], which is similar to the definition of V provided by *Ranney et al*. [2015]. Among such indices, SAVI was selected because it has been shown to be a reliable estimate of vegetation cover in areas with low vegetation density [*Purevdorj et al*., 1998] such as Reynolds Creek. Only three Landsat images (5 June 2013, 8 June 2014, and 11 June 2015) during the study period were free from cloud cover and therefore useable, so their SAVI values were averaged. The resulting fractional vegetation cover is shown in Figure 1b.

The EMT+VS model parameters were considered spatially constant and calibrated. In reality, soil properties might exhibit elevation dependence due to the elevation dependence of precipitation and PET over pedologic time scales. The feasible range for each parameter (Table 1) was determined from available information about the local soil, vegetation, and climatic characteristics [*Seyfried et al*., 2001]. For each case described later, the EMT+VS model was applied using two different calibration approaches. In the first approach, the parameter values were selected to maximize the average Nash-Sutcliffe coefficient of efficiency (NSCE) [*Nash and Sutcliffe*, 1970] for all dates in the soil moisture data set, similar to the procedure used by *Ranney et al*. [2015]. The calibrated parameter values for this case are shown in Table 1, but multiple parameter combinations can produce very similar performance. In a second approach, the available dates were divided into two halves, and the model was calibrated using one half of the data and validated using the other half of the data. This split-sample procedure was then repeated when the calibration and validation data sets were switched. Finally, an average performance measure was calculated for the calibration periods and another average was calculated for the validation periods.

4. Results

The analysis begins by assessing both the assumptions and the performance of the precipitation downscaling method. Then, the assumptions and performance of the PET downscaling method are evaluated. Finally, the effects of precipitation and PET variations on soil moisture downscaling are investigated. Unless otherwise noted, all precipitation and PET values discussed in the results are temporal averages calculated over the time periods with data (provided in the previous section). For clarity, we usually refer to these quantities as precipitation and PET and reserve the term average for other types of averages.

Table 1. Feasible Ranges for the Parameters Used in the EMT+VS Model Along With the Calibrated Values for Case 1 (the Preexisting EMT+VS Model), Case 2 (the Model With Precipitation Downscaling Included), and Case 3 (the Model With PET Downscaling Included)

	Ranges				
Parameter	Lower	Upper	Case 1	Case 2	Case 3
λ	0	0.99	0.63	0.92	0
η	0.01	1	0.01	1	0.63
μ	1	3	1	1.56	1.23
β_r	0.2	5	5	1.38	1.89
β_a	0.2	5	0.2	0.76	1.08
φ (m^3/m^3)	0.2	0.7	0.48	0.7	0.7
ι	1	500	276	319	500
$K_{s,v}$ (mm/d)	1	6228	3897	4052	2965
δ_0 (m)	1.2	1.2	1.2	1.2	1.2
κ_{min} (1/m)	−1000	−0.064	−889	−296	−391
ε	1	3	3	1.86	2.06
γ_v	1	29.92	9.73	20.11	25.39
γ_h	6.3	29.92	9.73	1.38	1.89
E_p (mm/d)	3.07	3.07	3.07	3.07	3.07
α	0.05	1.15	1.15	1.13	1.15
ω (1/m)	0	0.001	N/A	N/A	0.001
τ (1/m)	0	0.003	N/A	0.0013	N/A
ξ	0	2	N/A	1.18	N/A
ν (° from North)	0	360	N/A	149	N/A

4.1. Evaluation of Precipitation Downscaling

A key assumption in the precipitation downscaling method is that the relationships with topographic attributes occur at a scale that is coarser than the 30 m DEM. To evaluate this assumption, $Z_\#$, $S_\#$, and $R_\#$ were calculated for neighborhood sizes ranging from 30 m to 12 km. For each neighborhood size, regressions were performed between the observed precipitation at each station and both $Z_\#$ and $S_\#\cos\left(R_\#-\nu\right)$, which is how the orographic variables appear in the downscaling model. When performing these regressions, ν was selected to maximize each regression's coefficient of determination r^2. The curves in Figure 2 show the results of this analysis. Lower r^2 values are observed at small scales, but a noticeable peak occurs for both $Z_\#$ and $S_\#\cos\left(R_\#-\nu\right)$ at about 7 km. This spatial scale is similar to those identified by other researchers for other regions [*Thornton et al.*, 1997; *Sharples et al.*, 2005] and is therefore used in the remainder of this study. At the 7 km scale, ν is 64° from North, indicating that precipitation is highest on east-northeast facing slopes. The prevailing wind at Reynolds Creek comes from the west and southwest [*Hanson*, 1982], suggesting that precipitation is higher on the leeward side of the mountains.

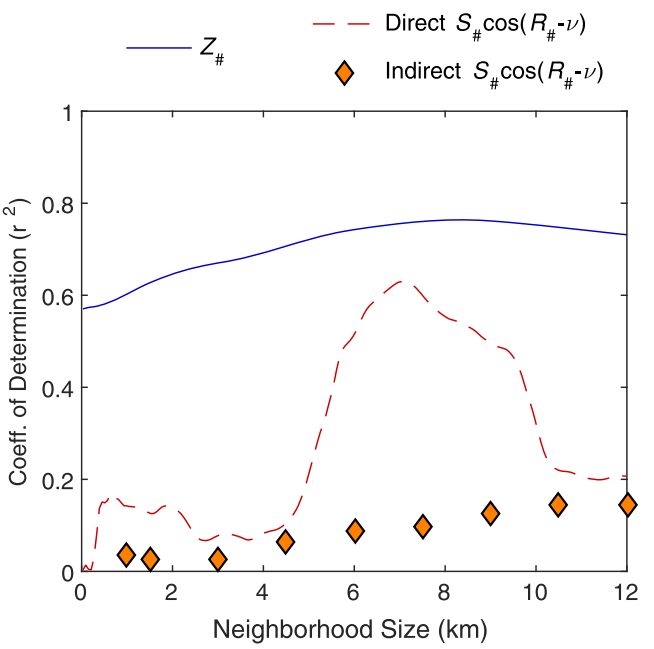

Figure 2. Strength of the relationship between temporally averaged precipitation at the rain gauge locations and the topographic attributes as the size of the neighborhood used to calculate the attributes changes. The graph also compares the direct and indirect methods for calculating the orographic orientation $S_\#\cos\left(R_\#-\nu\right)$. $Z_\#$ is the same for both methods.

Figure 2 also considers an alternative method for calculating $S_\#$ and $R_\#$. The method proposed earlier (called the direct method) first calculates fine resolution maps of slope and aspect from the fine resolution elevation data and then averages these attributes within the neighborhood to obtain $Z_\#$, $S_\#$,

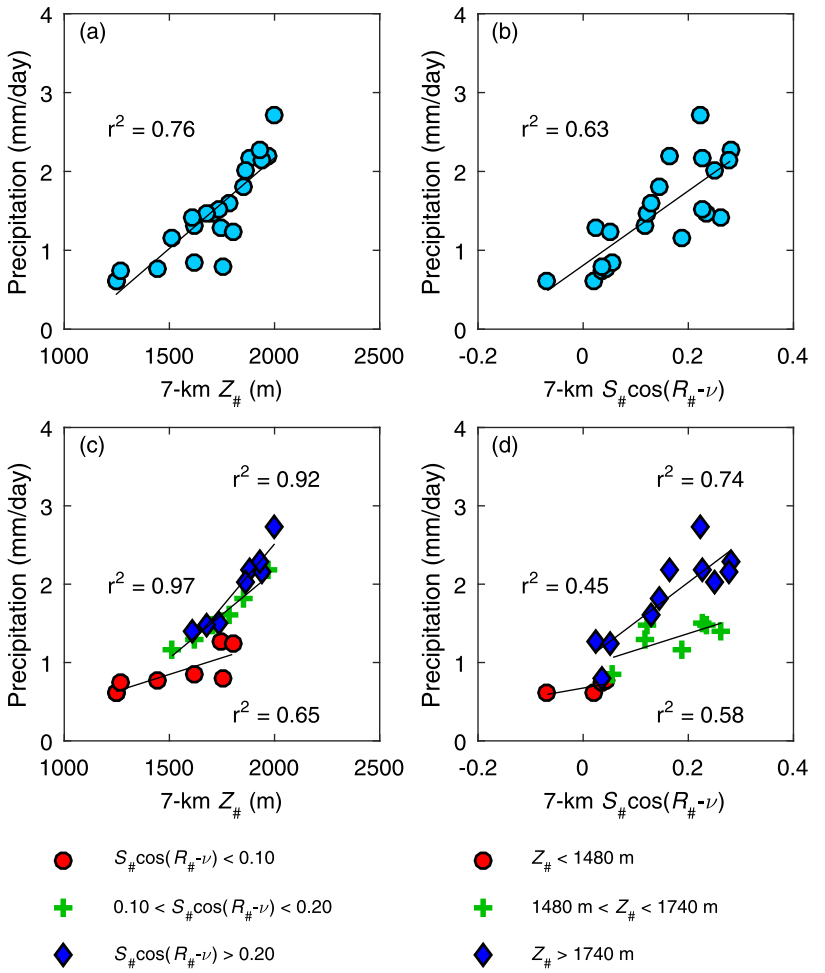

Figure 3. Relationships between temporally averaged precipitation at the rain gauge locations and (a) orographic elevation $Z_\#$, (b) orographic orientation $S_\#\cos(R_\#-\nu)$, (c) $Z_\#$ (when locations are grouped using ranges of $S_\#\cos(R_\#-\nu)$), and (d) $S_\#\cos(R_\#-\nu)$ (when locations are grouped using ranges of $Z_\#$). All topographic attributes are calculated using the direct method and a 7 km neighborhood.

and $R_\#$. The alternative method (called the indirect method) first averages the elevation values within each neighborhood to obtain $Z_\#$ and then uses $Z_\#$ to calculate $S_\#$ and $R_\#$. Figure 2 shows that the proposed (direct) method produces much stronger correlations between precipitation and the topographic data than the alternative (indirect) method. This result might also apply to other precipitation downscaling methods. One interpretation of this result is that local elevations, aspects, and slopes affect the production of precipitation, but due to horizontal air movement and translation of storms, the attributes are more informative when averaged over a larger (~7 km) scale.

Next, we evaluate the mathematical structure of the precipitation downscaling method. The method assumes precipitation is a linear function of $Z_\#$. Figure 3a plots the observed precipitation at each station against $Z_\#$ for a neighborhood size of 7 km. The precipitation changes by roughly 2.1 mm/d over the range of orographic elevations represented by the stations (roughly 750 m). Although some curvature is observed in the graph, the relationship is approximately linear and relatively strong ($r^2 = 0.76$). The downscaling model also assumes a linear relationship between precipitation and $S_\#\cos(R_\#-\nu)$. Figure 3b plots the observed precipitation at each station against $S_\#\cos(R_\#-\nu)$ for a neighborhood size of 7 km. High values of $S_\#\cos(R_\#-\nu)$ represent locations that have a strong slope in an east-northeast direction. Such stations have a precipitation of about 2.2 mm/d, but scatter is observed. Only one station has a slope in the opposite direction (a negative value of $S_\#\cos(R_\#-\nu)$). Its precipitation is approximately 0.6 mm/d. The relationship is approximately linear, and $r^2 = 0.63$. Finally, the downscaling model assumes that the dependence on elevation is affected by topographic orientation (and the dependence on orientation is affected by elevation).

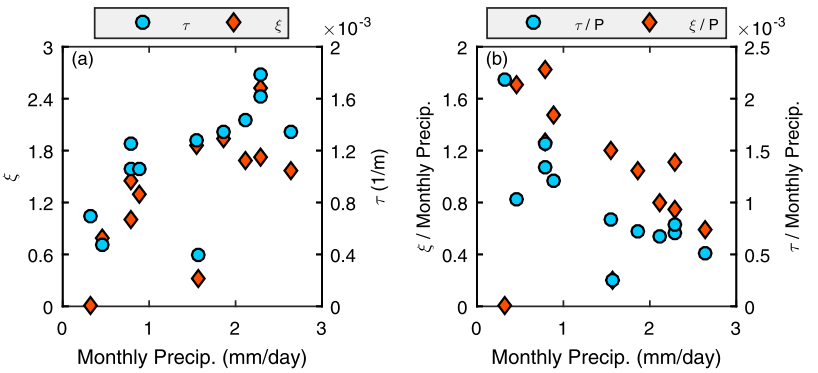

Figure 4. (a) Monthly ξ and τ values and (b) monthly ξ and τ values divided by the monthly average precipitation plotted against monthly average precipitation.

Figure 3c plots the relationship between the observed precipitation and $Z_\#$ when the data are divided into three ranges of $S_\#\cos\left(R_\#-v\right)$. The results show that the slope of the relationship with $Z_\#$ depends on the value of $S_\#\cos\left(R_\#-v\right)$. Furthermore, the dependence on $S_\#\cos\left(R_\#-v\right)$ explains the small curvature that was observed in Figure 3a. Similarly, Figure 3d plots the relationship between precipitation and $S_\#\cos\left(R_\#-v\right)$ when the data are divided into ranges of $Z_\#$. Consistent with the model formulation, the slope of the relationship with $S_\#\cos\left(R_\#-v\right)$ depends on the value of $Z_\#$.

The precipitation downscaling method also assumes that the slopes of the relationships with $Z_\#$ and $S_\#\cos\left(R_\#-v\right)$ are independent of the spatial average precipitation. This assumption is evaluated by calculating the slopes of those relationships (i.e., ξ and τ) for each month of the year and plotting those slopes as a function of the monthly average precipitation. For the data to be consistent with the model structure, ξ and τ should be the same for each month. Figure 4a shows that the monthly values of ξ and τ are quite variable (because the spatial patterns of individual storms vary), and the average becomes more sensitive to those individual patterns as the time period over which the average is calculated decreases. Weak increases in ξ and τ with precipitation seem to occur. Figure 4b examines an alternative approach where the relationship slopes are assumed to depend linearly on the spatial average precipitation. To be consistent with this alternative approach, the vertical coordinates in Figure 4b should be constant. Comparing Figures 4a and 4b, it is clear that the proposed model is superior to this alternative approach.

The overall performance of the proposed precipitation downscaling method is evaluated by comparing the downscaled (fine resolution) precipitation estimates with the values from the rain gauges. The input for the precipitation downscaling method is the space-time average precipitation rate for the watershed (1.46 mm/d), which was calculated from the rain gauges. The parameters τ, ξ, and v were calibrated to maximize the NSCE of the precipitation estimates compared with the observed precipitation values. Figure 5a plots the downscaled precipitation against the observations at the stations. The downscaling method captures the temporal average precipitation at the gauges very well (NSCE = 0.90). The ability of the method to capture individual storm patterns was not examined because the EMT+VS model does not consider temporal variability aside from $\overline{\theta}$. However, it is highly unlikely that the precipitation downscaling method can capture the spatial distribution of individual storms due to the wide variation in the spatial patterns of different storms.

To further evaluate the performance of the precipitation downscaling method, its results are compared to a map of average precipitation that was independently developed for the Reynolds Creek watershed by the United Sates Department of Agriculture-Agricultural Research Service (USDA-ARS). This data set is available from scholarworks.boisestate.edu/reynoldscreek/1/. For each time increment from 2012 through 2014, they used a detrended kriging procedure [*Garen et al.*, 1994] to estimate the precipitation pattern across the watershed. The method accounts for the nonstationarity due to orography with a linear relationship between precipitation and local elevation. The average precipitation map was then calculated from these kriged maps. For comparison, the precipitation downscaling method was applied to the entire watershed using the space-time average precipitation from the USDA-ARS map (1.11 mm/d) and by recalibrating the

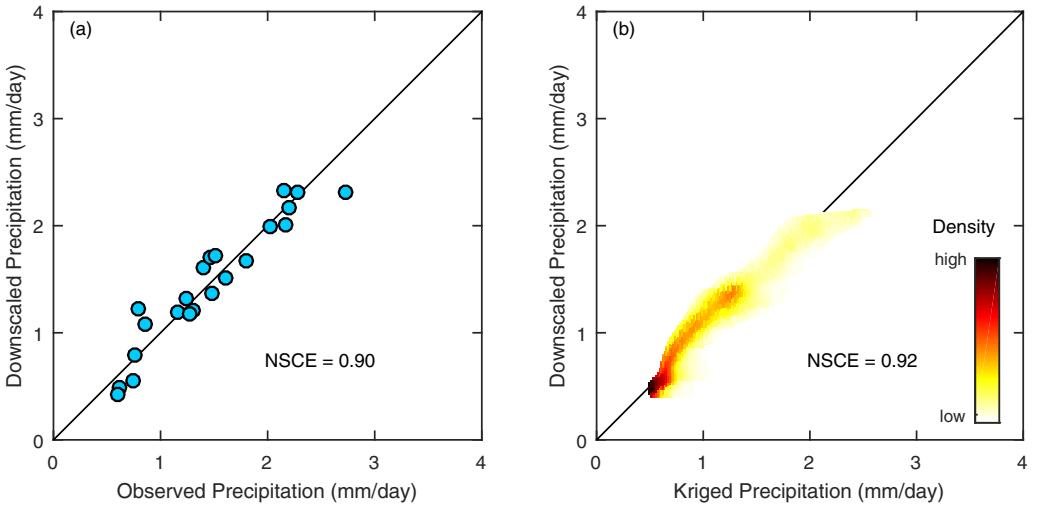

Figure 5. (a) Relationship between observed temporally averaged precipitation at rain gauge locations and EMT+VS downscaled average precipitation at the same locations. (b) Relationship between kriged average precipitation and downscaled precipitation for the entire watershed (using a density scatterplot where the density represents the number of data points at a given location in the plot).

parameters. Figure 5b compares the precipitation values from the USDA-ARS and downscaling methods. The downscaling method reproduces the USDA-ARS precipitation values very well (NSCE = 0.92).

Figure 6 shows the USDA-ARS precipitation map, the downscaled precipitation map, and the difference between the two maps. Both precipitation maps exhibit smaller precipitation values at the lower elevations (in the northern part of the watershed). However, the USDA-ARS map exhibits much more local variability in the precipitation because it uses fine resolution elevations in the kriging method. The downscaled map exhibits a much smoother pattern because it uses the topographic attributes from the 7 km scale. Despite their differences in appearance, the precipitation values are quite similar as shown in Figure 5b.

4.2. Evaluation of PET Downscaling

The PET downscaling method assumes that PET depends linearly on surface air temperature and that surface air temperature depends linearly on elevation. Together, these two assumptions imply that PET depends linearly on elevation. Figure 7 evaluates these assumptions using the P-M PET values calculated at each weather station. Figure 7a shows that an approximately linear relationship occurs between the temporal average PET and air temperature. However, much scatter is observed ($r^2 = 0.38$), which indicates that other variables substantially affect the PET at each station. Figure 7b shows that a strong linear relationship occurs between average air temperature and elevation at the stations ($r^2 = 0.89$). Over a range of about 970 m, the temperature changes by about 4.3°C. The resulting relationship between PET and elevation is shown in Figure 7c. Here again, substantial scatter is seen ($r^2 = 0.32$), but no obvious nonlinearity is visible. The scatter is not surprising because elevation alone is not expected to fully explain the spatial variation in PET. Over the range of elevations represented by the stations (roughly 970 m), the PET changes by about 1.4 mm/d. This change is about two thirds of the variation in precipitation of a similar range of elevation.

A key property of the PET downscaling method is that the slope of the relationship between Z and E_p depends both on ω and the spatial average PET $\overline{E}_p$ (see first term in parentheses in equation (16)). This assumption is evaluated by calculating the average PET at each station for each month of the year and then performing linear regressions between those monthly average PET values and elevation. For the data to be consistent with the model structure, the regression slopes should depend on the spatial average PET (i.e., $\overline{E}_p$) for each month. Figure 8a plots the regression slopes as a function of $\overline{E}_p$, and a clear increase is observed as $\overline{E}_p$ increases. These results can also be visualized by dividing each regression slope by $\overline{E}_p$ to calculate ω (Figure 8b). The results show that ω is relatively stable (near 0.0003 1/m) as $\overline{E}_p$ changes, which supports the model structure. Little scatter is observed when $\overline{E}_p$ is large, which suggests the relationship between PET and elevation is stronger and more stable during the summer months. The r^2 values also improve when $\overline{E}_p$ is large.

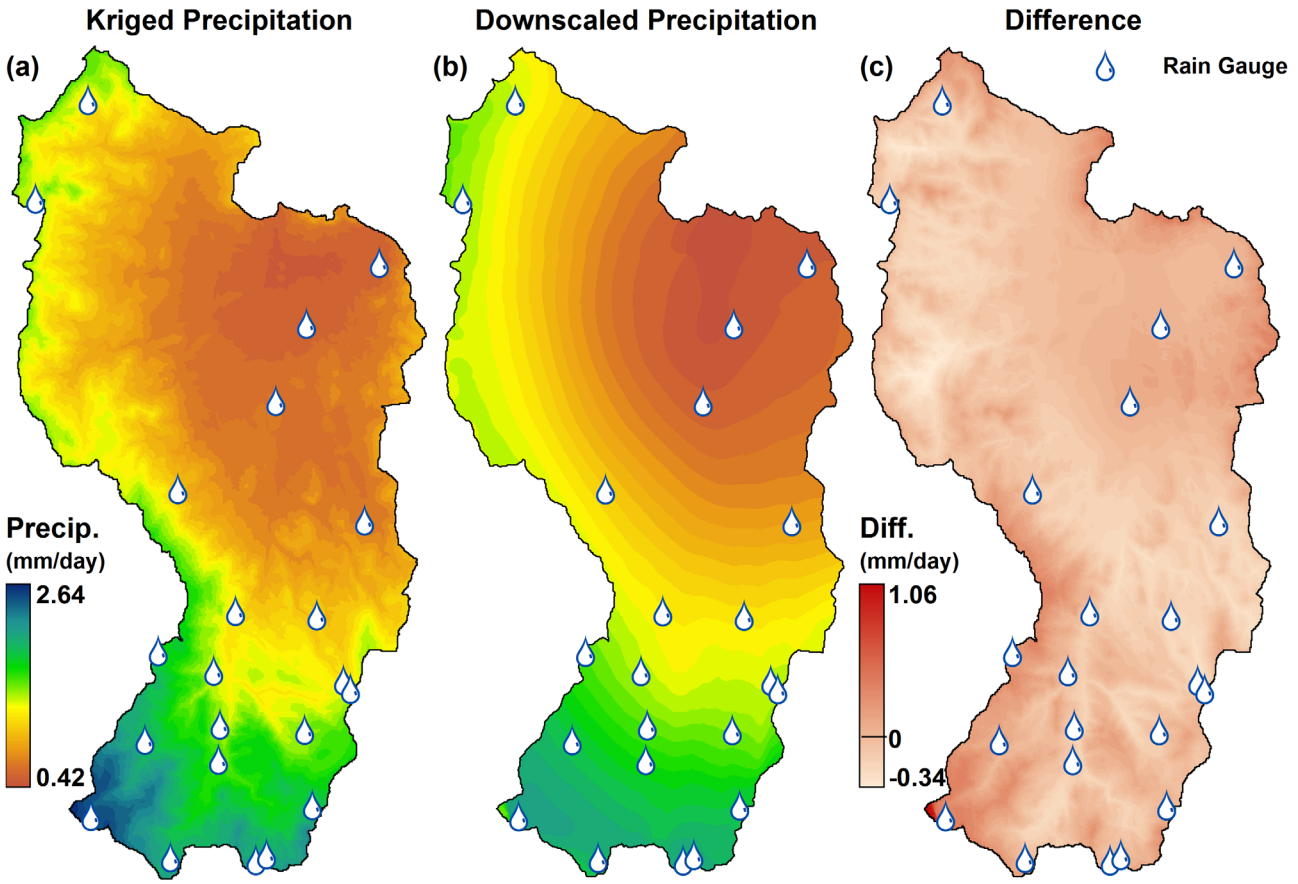

Figure 6. Maps of (a) Kriged temporally averaged precipitation, (b) average precipitation from the downscaling method, and (c) Kriged precipitation minus downscaled precipitation.

To quantify the performance of the PET downscaling method, the downscaled (fine resolution) PET values are compared to the P-M PET values at the weather stations. The input to the downscaling method ($\bar{E}_p$) is the spatial average P-M PET from the stations (2.8 mm/d). The parameter ω was calibrated to maximize the NSCE of the estimated PET values at the weather stations. The results (Figure 9a) show that the downscaling method only weakly captures the spatial variability in the P-M PET values (NSCE = 0.32). This result suggests that the downscaling method only gives an approximate estimate of local PET and has potential to be improved in the future by adding supplemental data. Likely, the weak relationship between PET and

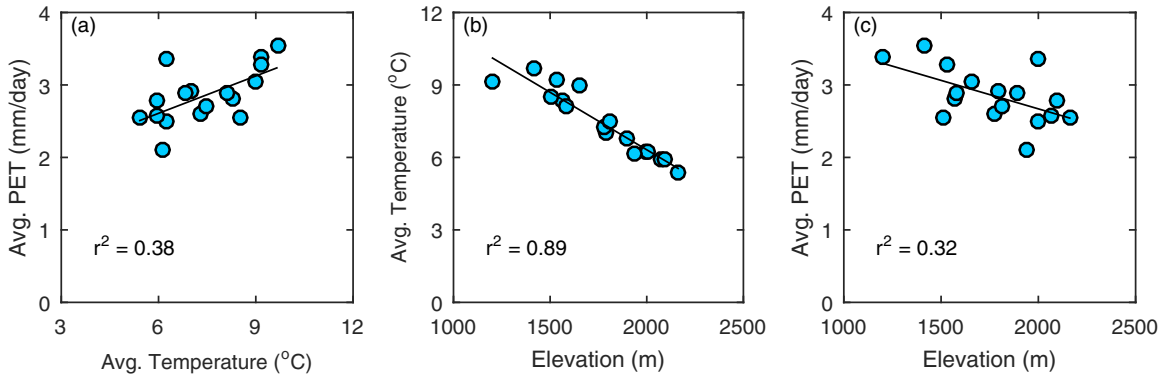

Figure 7. For weather station locations, relationships between (a) temporally averaged Penman-Monteith (P-M) PET and average air temperature, (b) average air temperature and elevation, and (c) average P-M PET and elevation.

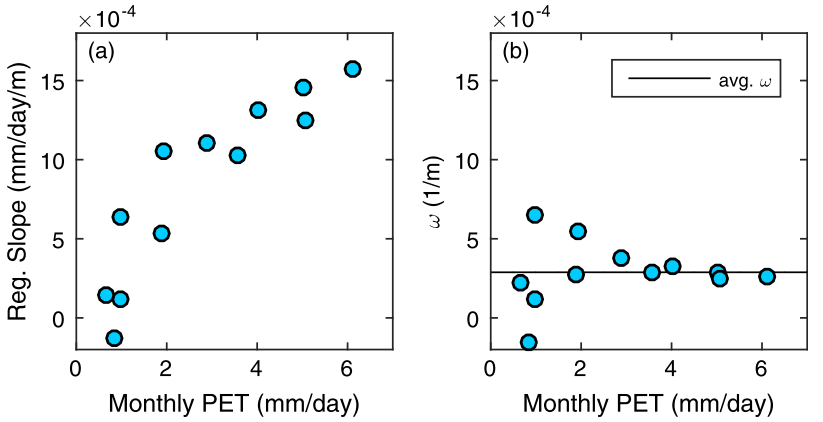

Figure 8. (a) Regression slopes of the relationship between monthly average Penman-Monteith (P-M) PET and elevation plotted against monthly average P-M PET, and (b) monthly ω values (parameter that partly controls the dependence of PET on elevation) plotted against monthly average P-M PET.

temperature that was observed earlier produces much of the scatter seen here. For example, variations in temperature do not capture spatial variations in wind speed.

Another potential hindrance in PET downscaling performance is the abandonment of the P-M equation for calculating local PET. The P-M equation is used to calculate the spatial average PET $\overline{E}_p$, which is supplied to the downscaling method, but P-M is not otherwise used. To consider this possibility, a PET map for the watershed was generated using the P-M equation. To calculate P-M PET at all locations, the weather station data were extrapolated throughout the watershed. The extrapolation was performed using a regression approach. All inputs for the P-M equation (temperature, incoming solar radiation, wind speed, relative humidity, and cloudiness) were plotted as functions of elevation to determine the variables that could be considered spatially constant and those that should be estimated using elevation. Temperature and relative humidity exhibit clear relationships with elevation (not shown here) and are allowed to vary each day. The other variables are approximately constant between locations (not shown), so spatial averages are used for each day. Using this approach, daily P-M PET maps were produced and used to calculate the temporal average P-M PET map. The P-M PET map was then compared to the downscaled (fine resolution) PET map. The downscaled PET map uses the spatial average P-M PET as input, and ω was calibrated to maximize the NSCE of the downscaled PET pattern (treating the P-M map as the observations). Figure 9b compares the

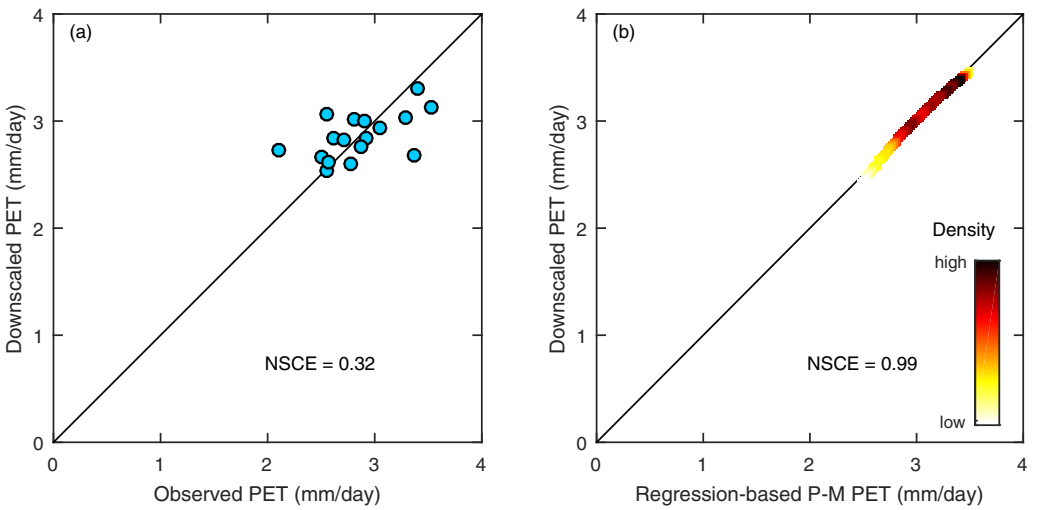

Figure 9. (a) Comparison of average Penman-Monteith (P-M) PET from weather station data and downscaled PET at the weather stations, and (b) comparison of regression-based P-M PET and downscaled PET for the entire watershed (using a density scatterplot where the density represents the number of data points at a given location in the plot).

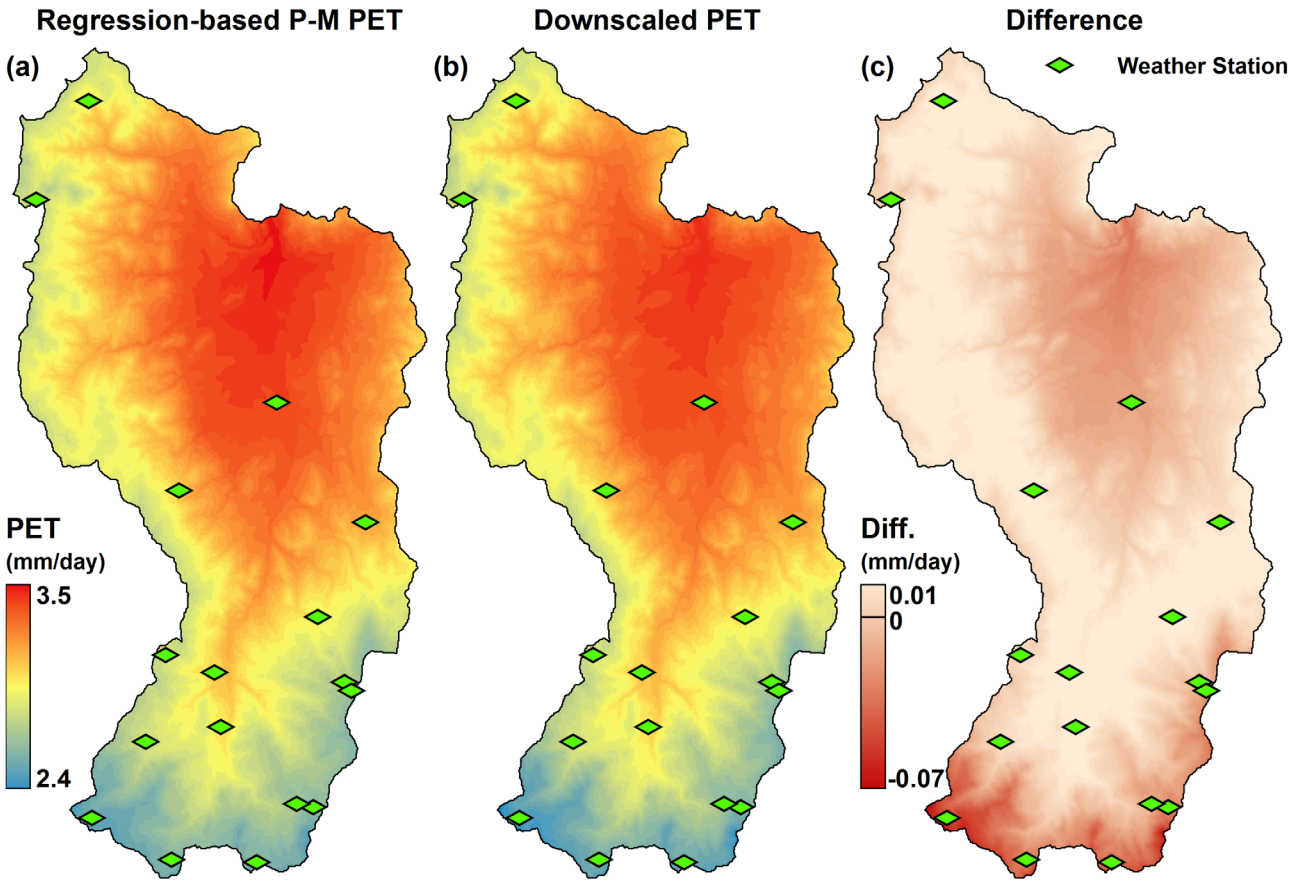

Figure 10. Maps of (a) average PET from the regression-based Penman-Monteith (P-M) method, (b) average PET from downscaling method, and (c) P-M PET minus downscaled PET.

PET values from the two methods at each location in the watershed. The two procedures provide very similar estimates of PET even though the downscaling method does not use the P-M equation at every location. The slight curvature of the data in the plot likely occurs because the downscaling method uses a linear dependence on temperature instead of the P-M equation. Figure 10 shows the two PET maps along with their difference. The largest differences occur at locations with extreme values of elevation. However, the maximum difference is only 3–5% of the estimated PET, which is why the two PET maps appear almost identical.

4.3. Effects of Precipitation and PET on Soil Moisture Downscaling

To investigate the impact that the precipitation and PET patterns have on soil moisture downscaling, three cases are compared. Case 1 uses the original EMT+VS model, so the only variables that produce spatial variations are V, S, κ, I_p, and A. Case 2 adds the precipitation downscaling method to the EMT+VS model. Thus, additional spatial variation can be produced by the orographic variables $Z_\#$, $S_\#$, and $R_\#$. Case 3 adds the PET downscaling method instead of the precipitation downscaling method. Thus, it is the same as the first case, but spatial variations can also be introduced by Z.

A typical soil moisture pattern for Case 1 is shown in Figure 11a. This date (2 June 2012) has intermediate moisture among those considered. Overall, the soil moisture pattern produces wetter conditions at high elevations even though elevation does not appear as a variable in the model. In this scenario, the calibrated parameters produce much of the spatial variation using vegetation cover. The vegetation shades the ground surface, reducing soil evaporation and increasing soil moisture in the model. Vegetation cover tends to be thicker at high elevations in the watershed (Figure 1b). However, in order for the EMT+VS model to capture the wet conditions at high elevations, this case over-estimates the dependence on vegetation. This over-dependence can be seen in the unrealistically wet conditions for the agricultural fields in the northern portion of the watershed. No soil moisture observations are available at these fields to constrain the model

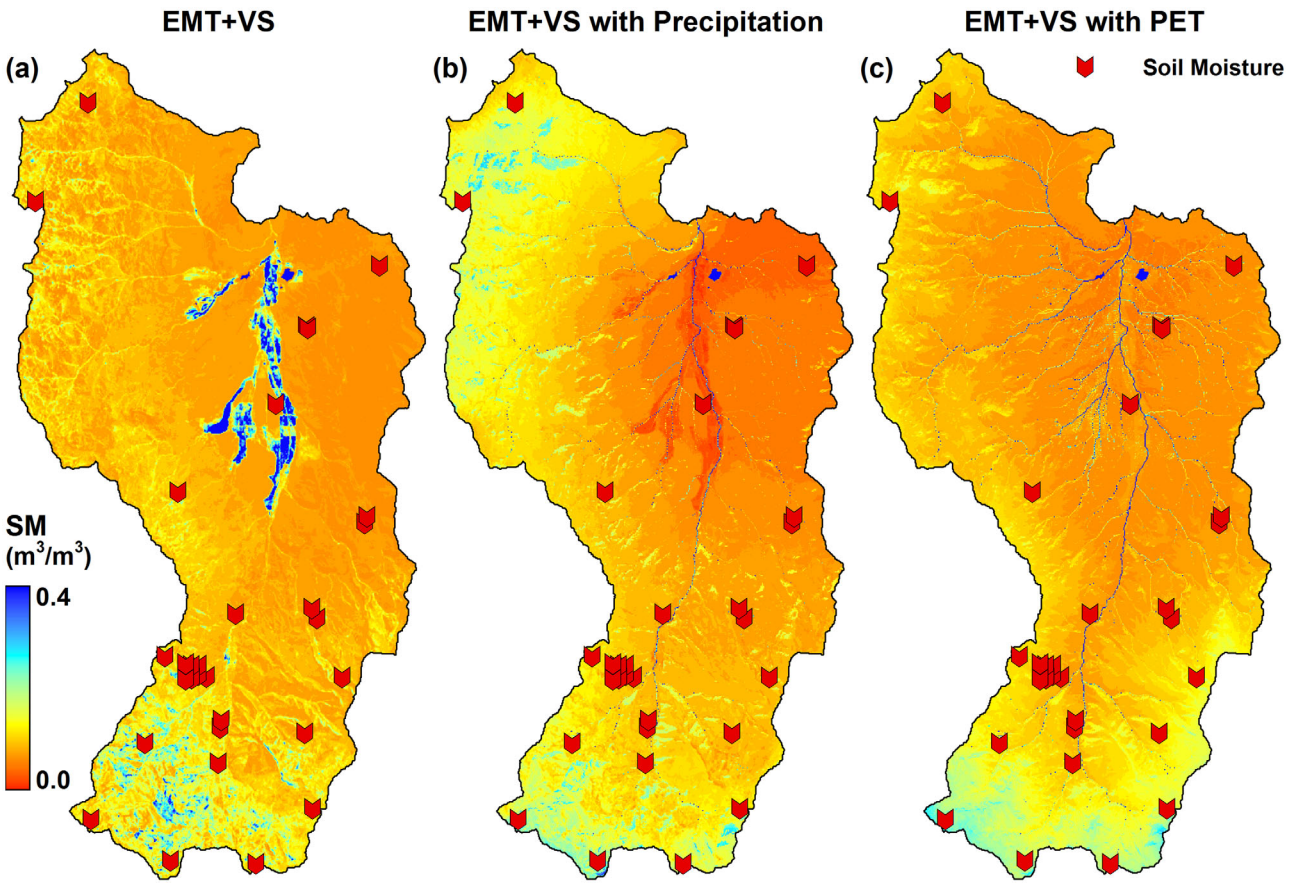

Figure 11. Downscaled soil moisture maps for 02 June 2012 from the Equilibrium Moisture from Topography, Vegetation, and Soil (EMT+VS) model when (a) the pre-existing EMT+VS model is used, (b) precipitation downscaling is included, and (c) PET downscaling is included.

behavior. Varying vegetation cover on opposing hillslopes throughout the watershed (Figure 1b) also allows the soil moisture pattern in Case 1 to show some hillslope (aspect) dependence.

Figure 11b shows the soil moisture pattern on the same date for Case 2 (precipitation downscaling is included). The soil moisture pattern exhibits a more obvious dependence on elevation than Case 1 with low elevation points exhibiting much less moisture than high elevation points. Additionally, the western side of the watershed is wetter than the eastern side due to the orographic orientation that is used in the model. The soil moisture pattern also produces saturated conditions at stream locations (even though soil moisture observations are not available at or near the streams). This feature is produced by the lateral flow term in the EMT+VS model. Unlike Case 1, thicker vegetation cover produces drier conditions in Case 2. The calibrated parameters suggest that interception and root water uptake reduce the soil moisture more than shading increases it. This behavior might be unrealistic because previous studies in semiarid watersheds have shown that vegetation cover is associated with greater soil moisture at shallow depths [*D'Odorico et al*., 2007; *Traff et al*., 2015]. Furthermore, this type of vegetation dependence predicts very dry conditions for the irrigated agricultural fields, which is also unlikely. This case also exhibits very strong aspect dependence, which is produced by spatial variations in insolation instead of vegetation cover.

Figure 11c shows the soil moisture pattern on the same date for Case 3 (PET downscaling is used instead of precipitation downscaling). Clear elevation dependence is again observed in the soil moisture pattern, and saturated conditions are again produced for stream locations. Here the dependence on vegetation is much weaker than Case 1, but wetter conditions are again produced for locations with thicker vegetation cover. The agricultural fields are wetter than nearby locations, but the wettest locations occur at high elevations. A moderate dependence on aspect is also produced for this case. The parameters indicate that a combination of lower PSRI values and thicker vegetation cover produces wetter conditions on north facing hillslopes.

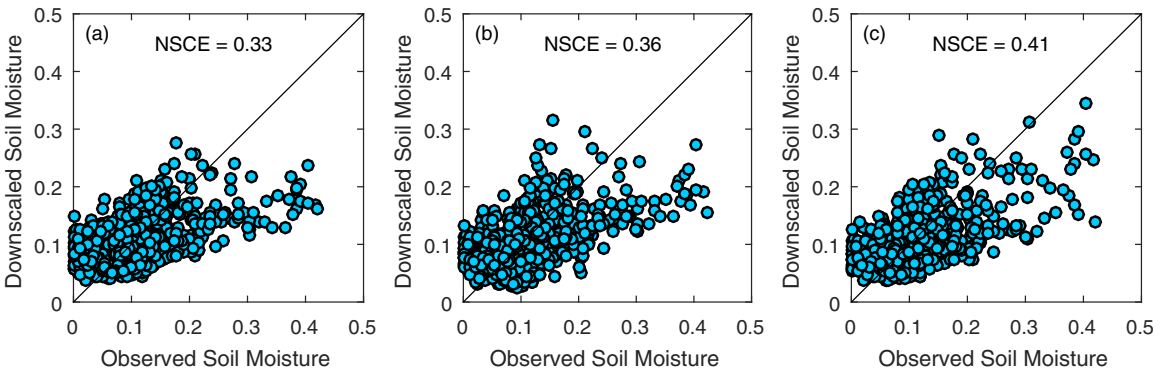

Figure 12. Comparisons of observed soil moisture and Equilibrium Moisture from Topography, Vegetation, and Soil (EMT+VS) model soil moisture estimates for all dates when: (a) the preexisting EMT+VS model is used, (b) precipitation downscaling is included, (c) PET downscaling is included. The NSCEs shown are the space-time values.

To evaluate the downscaling performance for all dates in the data set, the estimated soil moisture values are plotted against the in situ observations in Figure 12. For all three cases, the downscaled patterns typically underestimate the moisture at the wettest locations and overestimate the moisture at the drier locations (i.e., the variance in the downscaled soil moisture patterns is less than that of the observed soil moisture pattern). This behavior partly occurs because the downscaled pattern is calibrated to minimize the error in its soil moisture estimates. This approach discourages extreme estimates of soil moisture because they produce large errors if incorrect. Another reason for this behavior is the bias in the provided average soil moisture $\overline{\theta}$. Among the 30 soil moisture probes in the watershed, only 7 are located below the average watershed elevation. Thus, the average soil moisture from these probes is likely greater than the actual average for the watershed. The EMT+VS model always maintains the average it is provided, so a biased average causes the model to reduce the variance in its estimates to help it achieve higher NSCE values.

Comparing Figures 12a and 12b, the estimates of soil moisture appear to improve when precipitation downscaling is added to the model. The estimates appear to further improve when PET downscaling is used instead of precipitation downscaling (Figure 12c). Most notably, the wettest locations appear to be captured best when PET downscaling is used (Case 3). This visual interpretation is confirmed by metrics of model performance. If the NSCE is calculated for each downscaled pattern in the data set and then averaged, it is 0.19 for Case 1, which is comparable to previous applications of the EMT+VS model [*Ranney et al*., 2015]. If the NSCE is calculated for the entire space-time data set together, it is 0.33. When the precipitation downscaling method is included in Case 2, the average spatial NSCE for all dates increases to 0.24, and the space-time NSCE becomes 0.36. Comparing Case 2 to Case 1, the downscaling performance improves for 23 out of 30 dates. For Case 3, when PET downscaling is used instead of precipitation downscaling, the average spatial NSCE increases to 0.29, and the space-time NSCE becomes 0.41. Comparing Case 3 to Case 1, the performance improves for 27 out of 30 dates. Similar improvements are also observed if other measures of error are used (e.g., the root mean squared error). When the dates were split into calibration and validation samples, the results again suggest that precipitation and PET downscaling improve the estimation of soil moisture, with the PET downscaling method providing more improvement than the precipitation downscaling method. The average spatial calibration and validation NSCEs for Case 1 are 0.22 and 0.05, respectively. The average spatial NSCE values increase to 0.27 and 0.12 when the precipitation downscaling method is included for Case 2. For Case 3, the NSCE values increase to 0.32 and 0.20, respectively.

These results suggest that the precipitation and PET patterns affect the fine resolution patterns of soil moisture. Overall, the addition of PET downscaling improves the soil moisture estimates more than the addition of precipitation downscaling. This relative advantage of PET downscaling is surprising because the spatial variation in precipitation over the watershed is about 50% larger than the variation in PET. Furthermore, the spatial variation in average precipitation is better captured by the downscaling method than the spatial variation in average PET. However, the spatial patterns of individual precipitation events are expected to be highly variable. This variability is expected to be especially pronounced for the convective rain storms in May and June when the soil moisture patterns were downscaled, and *Garen et al*. [1994] found that the

relationship between precipitation and elevation at the Reynolds Creek Watershed is weaker in the summer months. Also, Figure 4a illustrated that the precipitation downscaling parameters ξ and τ can vary significantly from month to month. Thus, even though the precipitation downscaling method captures the average precipitation pattern in the watershed, this average pattern is weakly related to the soil moisture patterns. In contrast, the spatial pattern of PET is expected to be more persistent in time. For example, Figure 8b showed that ω is stable in summer months when PET is large, suggesting a strong relationship with elevation for this period. Thus, the PET downscaling method is less effective at capturing the average PET pattern, but it still provides greater benefit in downscaling soil moisture values.

Although not shown here, EMT+VS downscaling was performed when both the precipitation and PET downscaling methods were implemented. The results for this case are essentially unchanged from Case 3 when only PET downscaling is used. This behavior indicates that much of the soil moisture variability that can be captured by precipitation downscaling is already captured by PET downscaling. Both downscaling methods primarily introduce elevation dependence into the soil moisture patterns, so this overlap in the variance explained is not unexpected.

5. Conclusions

This study aimed to assess the impacts of variations in precipitation and PET on soil moisture downscaling for regions with large topographic relief. It introduced new downscaling methods for average precipitation and PET and implemented the new downscaling methods in the EMT+VS model. The following conclusions can be made:

1. The average spatial pattern of precipitation in Reynolds Creek is well estimated by the precipitation downscaling method. The downscaled precipitation values are similar to rain gauge values and the downscaled pattern is similar to the average pattern from detrended kriging of rain gauge data. The spatial pattern of precipitation depends on elevation and topographic orientation. The dependence on these topographic attributes is strongest when they are calculated at about a 7 km (orographic) scale, which is similar to the spatial scale found for other regions in previous studies. The precipitation has a linear relationship with elevation, but the slope of that relationship depends on the topographic orientation. Similarly, the precipitation has a linear relationship with topographic orientation, but the slope of that relationship depends on elevation.
2. The average spatial pattern of PET in Reynolds Creek can be approximated using the proposed PET downscaling method, but the PET downscaling method is less accurate than the precipitation downscaling method. When compared to P-M PET values from weather station data, the PET downscaling method only captures the general trend in PET. However, when the downscaled pattern is compared to a P-M PET pattern that is extrapolated from the weather station data, the two methods provide almost identical results. This similarity suggests that the full P-M equation is not needed for PET downscaling. At Reynolds Creek, the PET has a weak linear relationship with average air temperature, and average air temperature has a strong linear relationship with elevation. Together, these relationships produce a weak linear relationship between the average PET pattern and elevation.
3. Including orographic precipitation in the soil moisture downscaling method improves the estimates of surface soil moisture for Reynolds Creek. The average spatial NSCE of the soil moisture estimates increases from 0.19 to 0.24 when the precipitation downscaling is added to the model. Reynolds Creek has large topographic relief, and the precipitation varies substantially with elevation. The downscaling model is relatively successful at capturing the spatial pattern in average precipitation. However, precipitation downscaling provides a relatively small improvement in the soil moisture estimates likely because individual storm patterns differ, particularly in the summer when the soil moisture was downscaled.
4. Including elevation-dependent PET in the soil moisture downscaling method also improves the estimates of surface soil moisture for Reynolds Creek. When PET downscaling is added to the EMT+VS model, the average spatial NSCE increases from 0.19 to 0.29. For this watershed, PET downscaling provides a larger improvement in the soil moisture estimates than precipitation downscaling. The average PET varies less with elevation than the average precipitation, and the PET downscaling method is less successful than the precipitation downscaling method. However, the PET pattern is more persistent in time than the precipitation pattern, particularly in summer, so it has a stronger relationship with the soil moisture patterns.

5. When both precipitation and PET downscaling are used, the soil moisture results are essentially the same as when only PET downscaling is used. However, including precipitation downscaling requires three more parameters than using PET downscaling alone. Thus, using only PET downscaling might be appropriate for some watersheds where limited data are available to calibrate the model parameters.

Overall, this study shows that elevation should be included as a relevant topographic attribute when downscaling soil moisture in regions with large relief. The dependence on elevation has been neglected in several previous topographic downscaling studies because they focused on catchments with low relief. This study also identifies two physical mechanisms (precipitation and PET) through which elevation can affect soil moisture patterns, and it provides simple downscaling methods for precipitation and PET, which introduce elevation into the soil moisture downscaling model. Those downscaling methods also have potential applications beyond soil moisture downscaling.

Future research should consider additional application regions. The relative roles of precipitation and PET in determining the soil moisture patterns may change for more humid regions where average precipitation exceeds average PET. In addition, regions with more persistent orographic precipitation effects may demonstrate a stronger dependence than what was observed here. Furthermore, this study focuses only on the average precipitation and PET patterns because the EMT+VS includes an equilibrium assumption. However, the results suggest that orographic effects might be seasonal. If possible, the performance of the EMT+VS model should be evaluated when temporal variability is included in more inputs than the spatial average soil moisture. Finally, the propagation of errors in the supplied soil moisture values to the fine-scale soil moisture patterns should also be examined.

Acknowledgments

The authors acknowledge the Army Research Laboratory (ARL) Small Business Innovative Research (SBIR) program for their financial support. We would like to thank Patrick Kormos from the Agricultural Research Service for providing the kriged precipitation map for the Reynolds Creek Watershed. We would also like to thank Dylan Hoehn for his technical support and helpful suggestions throughout the study and four anonymous reviewers for their recommendations. Data from this work can be obtained by contacting Jeffrey Niemann at jniemann@engr.colostate.edu.

References

ASCE-EWRI (2005), The ASCE standardized reference evapotranspiration equation, final report, Environ. and Water Resour. Inst. of the Am. Soc. of Civ. Eng., Reston, Va.

Basist, A., G. D. Bell, and V. Meentemeyer (1994), Statistical relationships between topography and precipitation patterns, *J. Clim.*, *7*(9), 1305–1315.

Beven, K. J., and M. J. Kirkby (1979), A physically based, variable contributing area model of basin hydrology, *Hydrol. Sci. Bull.*, *24*(1), 43–69.

Blaney, H. F., and W. D. Criddle (1950), Determining water requirements in irrigated areas from climatological and irrigation data, *USDA SCS-TP-96*, U.S. Dept. of Agric., Washington, D. C.

Bras, R. L. (1990), *Hydrology: An Introduction to Hydrologic Science*, Addison-Wesley, Boston, Mass.

Brocca, L., R. Morbidelli, F. Melone, and T. Moramarco (2007), Soil moisture spatial variability in experimental areas of central Italy, *J. Hydrol.*, *333*(2–4), 356–373.

Campbell, G. S. (1974), Simple method for determining unsaturated conductivity from moisture retention data, *Soil Sci.*, *117*(6), 311–314.

Castillo, V. M., A. Gomez-Plaza, and M. Martinez-Mena (2003), The role of antecedent soil water content in the runoff response of semiarid catchments: A simulation approach, *J. Hydrol.*, *284*(1–4), 114–130.

Castro, L. M., J. Gironás, and B. Fernández (2014), Spatial estimation of daily precipitation in regions with complex relief and scarce data using terrain orientation, *J. Hydrol.*, *517*, 481–492.

Chauhan, N. S., S. Miller, and P. Ardanuy (2003), Spaceborne soil moisture estimation at high resolution: A microwave-optical/IR synergistic approach, *Int. J. Remote Sens.*, *24*(22), 4599–4622.

Chua, S., and R. L. Bras (1982), Optimal estimators of mean areal precipitation in regions of orographic influence, *J. Hydrol.*, *57*(1–2), 23–48.

Coleman, M. L., and J. D. Niemann (2013), Controls on topographic dependence and temporal instability in catchment-scale soil moisture patterns, *Water Resour. Res.*, *49*, 1625–1642, doi:10.1002/wrcr.20159.

Crow, W. T., E. F. Wood, and R. Dubayah (2000), Potential for downscaling soil moisture maps derived from spaceborne imaging radar data, *J. Geophys. Res.*, *105*(2), 2203–2212.

Daly, C., R. P. Neilson, and D. L. Phillips (1994), A statistical topographic model for mapping climatological precipitation over mountainous terrain, *J. Appl. Meteorol.*, *33*(2), 140–158.

Das, N. N., D. Entekhabi, E. G. Njoku, J. J. C. Shi, J. T. Johnson, and A. Colliander (2014), Tests of the SMAP combined radar and radiometer algorithm using airborne field campaign observations and simulated data, *IEEE Trans. Geosci. Remote Sensing*, *52*(4), 2018–2028.

D'Odorico, P., K. Caylor, G. S. Okin, and T. M. Scanlon (2007), On soil moisture-vegetation feedbacks and their possible effects on the dynamics of dryland ecosystems, *J. Geophys. Res.*, *112*, G04010, doi:10.1029/2006JG000379.

Dodson, R., and D. Marks (1997), Daily air temperature interpolated at high spatial resolution over a large mountainous region, *Clim. Res.*, *8*(1), 1–20.

Doorenbos, J., and W. O. Pruitt (1977), Guidelines for prediction of crop water requirements, FAO Irrig. Drain. Pap. 24, Food and Agric. Organ. of the U. N., Rome.

Ekström, M., P. D. Jones, H. J. Fowler, G. Lenderink, T. A. Buishand, and D. Conway (2007), Regional climate model data used within the SWURVE project 1: Projected changes in seasonal patterns and estimation of PET, *Hydrol. Earth Syst. Sci.*, *11*(3), 1069–1083.

Entekhabi, D., I. Rodriguez-Iturbe, and F. Castelli (1996), Mutual interaction of soil moisture state and atmospheric processes, *J. Hydrol.*, *184*(1–2), 3–17.

Entekhabi, D., et al. (2010), The soil moisture active passive (SMAP) mission, *Proc. IEEE*, *98*(5), 704–716.

Figa-Saldana, J., J. J. W. Wilson, E. Attema, R. Gelsthorpe, M. R. Drinkwater, and A. Stoffelen (2002), The advanced scatterometer (ASCAT) on the meteorological operational (MetOp) platform: A follow on for European wind scatterometers, *Can. J. Remote Sens.*, *28*(3), 404–412.

Foresti, L., and A. Pozdnoukhov (2012), Exploration of alpine orographic precipitation patterns with radar image processing and clustering techniques, *Meteorol. Appl.*, *19*(4), 407–419.

Franke, J., J. Häntzschel, V. Goldberg, and C. Bernhofer (2008), Application of a trigonometric approach to the regionalization of precipitation for a complex small-scale terrain in a GIS environment, *Meteorol. Appl.*, *15*(4), 483–490.
Garen, D. C., G. L. Johnson, and C. L. Hanson (1994), Mean areal precipitation for daily hydrologic modeling in mountainous regions, *Water Resour. Bull.*, *30*(3), 481–491.
Glenn, E. P., A. R. Huete, P. L. Nagler, and S. G. Nelson (2008), Relationship between remotely-sensed vegetation indices, canopy attributes and plant physiological processes: What vegetation indices can and cannot tell us about the landscape, *Sensors*, *8*(4), 2136–2160.
Gomez-Plaza, A., M. Martinez-Mena, J. Albaladejo, and V. M. Castillo (2001), Factors regulating spatial distribution of soil water content in small semiarid catchments, *J. Hydrol.*, *253*(1–4), 211–226.
Goovaerts, P. (2000), Geostatistical approaches for incorporating elevation into the spatial interpolation of rainfall, *J. Hydrol.*, *228*(1–2), 113–129.
Green, T. R., and R. H. Erskine (2004), Measurement, scaling, and topographic analyses of spatial crop yield and soil water content, *Hydrol. Processes*, *18*(8), 1447–1465.
Guan, H., J. L. Wilson, and O. Makhnin (2005), Geostatistical mapping of mountain precipitation incorporating autosearched effects of terrain and climatic characteristics, *J. Hydrometeorol.*, *6*(6), 1018–1031.
Hanson, C. L. (1982), Distribution and stochastic generation of annual and monthly precipitation on a mountainous watershed in southwest Idaho, *Water Resour. Bull.*, *18*(5), 875–883.
Hanson, C. L. (1989), Prediction of class A pan evaporation in southwest Idaho, *J. Irrig. Drain. Eng.*, *115*(2), 166–171.
Hanson, C. L. (2001), Long-term precipitation database, Reynolds Creek Experimental Watershed, Idaho, United States, *Water Resour. Res.*, *37*(11), 2831–2834.
Hevesi, J. A., J. D. Istok, and A. L. Flint (1992), Precipitation estimation in mountainous terrain using multivariate geostatistics: 1. Structural-analysis, *J. Appl. Meteorol.*, *31*(7), 661–676.
Huete, A. R. (1988), A soil-adjusted vegetation index (Savi), *Remote Sens. Environ.*, *25*(3), 295–309.
Itenfisu, D., R. L. Elliot, R. G. Allen, and I. A. Walter (2003), Comparison of reference evapotranspiration calculations as part of the ASCE standardization effort, *J. Irrig. Drain. Eng.*, *129*(6), 440–448.
Jawson, S. D., and J. D. Niemann (2006), Spatial patterns from EOF analysis of soil moisture at a large scale and their dependence on soil, land-use, and topographic properties, *Adv. Water Resour.*, *30*(3), 366–381.
Kaheil, Y. H., M. K. Gill, M. Mckee, L. A. Bastidas, and E. Rosero (2008), Downscaling and assimilation of surface soil moisture using ground truth measurements, *IEEE Trans. Geosci. Remote Sensing*, *46*(5), 1375–1384.
Kim, G., and A. P. Barros (2002), Downscaling of remotely sensed soil moisture with a modified fractal interpolation method using contraction mapping and ancillary data, *Remote Sens. Environ.*, *83*(3), 400–413.
Kyriakidis, P. C., and J. Kim, and N. L. Miller (2001), Geostatistical mapping of precipitation from rain gauge data using atmospheric and terrain characteristics, *J. Appl. Meteorol.*, *40*(11), 1855–1877.
Leemans, R., and W. P. Cramer (1991), The IIASA database for mean monthly values of temperature, precipitation, and cloudiness on a global terrestrial grid, *IIASA Res. Rep. RR-91-018*, Int. Inst. for Appl. Syst. Anal., Laxenburg, Austria.
Legates, D. R., R. Mahmood, D. F. Levia, T. L. DeLiberty, S. M. Quiring, C. Houser, and F. E. Nelson (2011), Soil moisture: A central and unifying theme in physical geography, *Prog. Phys. Geogr.*, *35*(1), 65–86.
Li, L., P. W. Gaiser, B. Gao, R. M. Bevilacqua, T. J. Jackson, E. G. Njoku, C. Rudiger, J. Calvet, and R. Bindlish (2010), WindSat global soil moisture retrieval and validation, *IEEE Trans. Geosci. Remote Sensing*, *48*(5), 2224–2241.
Lloyd, C. D. (2005), Assessing the effect of integrating elevation data into the estimation of monthly precipitation in Great Britain, *J. Hydrol.*, *308*(1–4), 128–150.
Ly, S., C. Charles, and A. Degre (2011), Geostatistical interpolation of daily rainfall at catchment scale: The use of several variogram models in the Ourthe and Ambleve catchments, Belgium, *Hydrol. Earth Syst. Sci.*, *15*(7), 2259–2274.
Mascaro, G., E. R. Vivoni, and R. Deidda (2010), Downscaling soil moisture in the southern Great Plains through a calibrated multifractal model for land surface modeling applications, *Water Resour. Res.*, *46*, W08546, doi:10.1029/2009WR008855.
Merlin, O., A. G. Chehbouni, Y. H. Kerr, E. G. Njoku, and D. Entekhabi (2005), A combined modeling and multi-spectral/multi-resolution remote sensing approach for disaggregation of surface soil moisture: Application to SMOS configuration, *IEEE Trans. Geosci. Remote Sens.*, *43*(9), 2036–2050.
Merlin, O., A. G. Chehbouni, Y. H. Kerr, and D. C. Goodrich (2006), A downscaling method for distributing surface soil moisture within a microwave pixel: Application to the Monsoon '90 data, *Remote Sens. Environ.*, *101*, 379–389.
Nash, J. E., and J. V. Sutcliffe (1970), River flow forecasting through conceptual models, part I—A discussion of principles, *J. Hydrol.*, *10*(3), 282–290.
Njoku, E. G., T. J. Jackson, V. Lakshmi, T. K. Chan, and S. V. Nghiem (2003), Soil moisture retrieval from AMSR-E, *IEEE Trans. Geosci. Remote Sens.*, *41*(2), 215–229.
Oudin, L., F. Hervieu, C. Michel, C. Perrin, V. Andreassian, F. Anctil, and C. Loumagne (2005), Which potential evapotranspiration input for a lumped rainfall-runoff model? Part 2—Towards a simple and efficient potential evapotranspiration model for rainfall-runoff modelling, *J. Hydrol.*, *303*(1–4), 290–306.
Pal, J. S., and E. A. B. Eltahir (2001), Pathways relating soil moisture conditions to future summer rainfall within a model of the land-atmosphere system, *J. Clim.*, *14*(6), 1227–1242.
Pellenq, J., J. Kalma, G. Boulet, G. M. Saulnier, S. Wooldridge, Y. Kerr, and A. Chehbouni (2003), A disaggregation scheme for soil moisture based on topography and soil depth, *J. Hydrol.*, *276*(1–4), 112–127.
Peng, J., A. Loew, S. Zhang, J. Wang, and J. Niesel (2016), Spatial downscaling of satellite soil moisture data using a vegetation temperature condition index, *IEEE Trans. Geosci. Remote Sens.*, *54*(1), 558–566.
Phillips, D. L., J. Dolph, and D. Marks (1992), A comparison of geostatistical procedures for spatial analysis of precipitation in mountainous terrain, *Agric. For. Meterol.*, *58*(1–2), 119–141.
Priestley, C. H. B., and R. J. Taylor (1972), Assessment of surface heat-flux and evaporation using large-scale parameters, *Mon. Weather Rev.*, *100*(2), 81–92.
Prudhomme, C., and D. W. Reed (1999), Mapping extreme rainfall in a mountainous region using geostatistical techniques: A case study in Scotland, *Int. J. Climatol.*, *19*(12), 1337–1356.
Purevdorj, T., R. Tateishi, T. Ishiyama, and Y. Honda (1998), Relationships between percent vegetation cover and vegetation indices, *Int. J. Remote Sens.*, *19*(18), 3519–3535.
Qiu, J., X. Mo, S. Liu, and Z. Lin (2014), Exploring spatiotemporal patterns and physical controls of soil moisture at various spatial scales, *Theor. Appl. Climatol.*, *118*(1–2), 159–171.

Ranney, K. J., J. D. Niemann, B. M. Lehman, T. R. Green, and A. S. Jones (2015), A method to downscale soil moisture to fine resolutions using topographic, vegetation, and soil data, *Adv. Water Resour.*, *76*, 81–96.
Rolland, C. (2003), Spatial and seasonal variations of air temperature lapse rates in Alpine regions, *J Clim.*, *16*(7), 1032–1046.
Ruggenthaler, R., F. Schoberl, G. Markart, K. Klebinder, A. Hammerle, and G. Leitinger (2015), Quantification of soil moisture effects on runoff formation at the hillslope scale, *J. Irrig. Drain. Eng.*, *141*(9), 1–14.
Seyfried, M. (1998), Spatial variability constraints to modeling soil water at different scales, *Geoderma*, *85*(2–3), 231–254.
Seyfried, M., R. Harris, D. Marks, and B. Jacob (2001), Geographic database, Reynolds Creek Experimental Watershed, Idaho, United States, *Water Resour. Res.*, *37*(11), 2825–2829.
Seyfried, M. S., and M. D. Murdock (2004), Measurement of soil water content with a 50-MHz soil dialectric sensor, *Soil Sci. Soc. Am. J.*, *68*, 394–403.
Seyfried, M. S., L. E. Grant, E. Du, and K. Humes (2005), Dielectric loss and calibration of the hydra probe soil water sensor, *Vadose Zone J.*, *4*(4), 1070–1079.
Seyfried, M., D. Chandler, and D. Marks (2011), Long-term soil water trends across a 1000-m elevation gradient, *Vadose Zone J.*, *10*(4), 1276–1286.
Sharples, J. J., M. F. Hutchinson, and D. R. Jellett (2005), On the horizontal scale of elevation dependence of Australian monthly precipitation, *J. Appl. Meteorol.*, *44*(12), 1850–1865.
Shevenell, L. (1999), Regional potential evapotranspiration in arid climates based on temperature, topography and calculated solar radiation, *Hydrol. Processes*, *13*(4), 577–596.
Shi, H. Y., X. D. Fu, J. Chen, G. Q. Wang, and T. J. Li (2014), Spatial distribution of monthly potential evaporation over mountainous regions: Case of the Lhasa River basin, China, *Hydrol. Sci. J.*, *59*(10), 1856–1871.
Singh, H. V., and A. M. Thompson (2016), Effect of antecedent soil moisture content on soil critical shear stress in agricultural watersheds, *Geoderma*, *262*, 165–173.
Song, C. Y., L. Jia, and M. Menenti (2014), Retrieving high-resolution surface soil moisture by downscaling AMSR-E brightness temperature using MODIS LST and NDVI data, *IEEE J. Stars*, *7*(3), 935–942.
Sperna Weiland, F. C., C. Tisseuil, H. H. Durr, M. Vrac, and L. P. H. van Beek (2012) Selecting the optimal method to calculate daily global reference potential evaporation from CSFR reanalysis data for application in a hydrological model study, *Hydrol. Earth Syst. Sci.*, *16*(3), 983–1000.
Spreen, W. C. (1947), A determination of the effect of topography upon precipitation, *Eos Trans. AGU*, *28*(2), 285–290.
Sun, R. H., and B. P. Zhang (2016), Topographic effects on spatial pattern of surface air temperature in complex mountain environment, *Environ. Earth Sci.*, *75*(7), 621.
Tarboton, D. G. (1997), A new method for the determination of flow directions and upslope areas in grid digital elevation models, *Water Resour. Res.*, *33*(2), 309–319.
Temimi, M., R. Leconte, N. Chaouch, P. Sukumal, R. Khanbilvardi, and F. Brissette (2010), A combination of remote sensing data and topographic attributes for the spatial and temporal monitoring of soil wetness, *J. Hydrol.*, *388*(1–2), 28–40.
Thornton, P. E., S. W. Running, and M. A. White (1997), Generating surfaces of daily meteorological variables over large regions of complex terrain, *J. Hydrol.*, *190*(3–4), 214–251.
Traff, D. C., J. D. Niemann, S. A. Middlekauff, and B. M. Lehman (2015), Effects of woody vegetation on shallow soil moisture at a semiarid montane catchment, *Ecohydrology*, *8*(5), 935–947.
Vanderlinden, K., J. V. Giraldez, and M. Van Meirvenne (2008), Spatial estimation of reference evapotranspiration in Andalusia, Spain, *J. Hydrometeorol.*, *9*(2), 242–255.
Werbylo, K. L., and J. D. Niemann (2014), Evaluation of sampling techniques to characterize topographically-dependent variability for soil moisture downscaling, *J. Hydrol.*, *516*, 304–316.
Western, A. W., R. B. Grayson, G. Bloschl, G. R. Willgoose, and T. A. McMahon (1999), Observed spatial organization of soil moisture and its relation to terrain indices, *Water Resour. Res.*, *35*(3), 797–810.
Western, A. W., G. Bloschl, and R. B. Grayson (2001), Toward capturing hydrologically significant connectivity in spatial patterns, *Water Resour. Res.*, *37*(1), 83–97.
Willmott, C. J., and K. Matsuura (1995), Smart interpolation of annually averaged air-temperature in the United States, *J. Appl. Meteorol.*, *34*(12), 2577–2586.
Wilson, D. J., A. W. Western, and R. B. Grayson (2005), A terrain and data-based method for generating the spatial distribution of soil moisture, *Adv. Water Resour.*, *28*(1), 43–54.